Basin Research
EAGE

Basin Research (2013) **25**, 388–418, doi: 10.1111/bre.12004

Stratigraphy and $^{40}Ar/^{39}Ar$ geochronology of the Santa Rosa basin, Baja California: Dynamic evolution of a constrictional rift basin during oblique extension in the Gulf of California

C. Seiler,* M.C. Quigley,† J.M. Fletcher,‡ D. Phillips,* A.J.W. Gleadow* and B.P. Kohn*

*School of Earth Sciences, The University of Melbourne, Victoria, 3010, Australia
†Department of Geological Sciences, University of Canterbury, Christchurch, 8140, New Zealand
‡Departamento de Geología, CICESE, Carr. Tijuana-Ensenada No.3918, Ensenada, BC, 22860, México

ABSTRACT

The Santa Rosa basin of northeastern Baja California is one of several transtensional basins that formed during Neogene oblique opening of the Gulf of California. The basin comprises Late Miocene to Pleistocene sedimentary and volcanic strata that define an asymmetric half-graben above the Santa Rosa detachment, a low-angle normal fault with *ca*. 4–5 km of SE-directed displacement. Stratigraphic analysis reveals systematic basin-scale facies variations both parallel and across the basin. The basin-fill exhibits an overall fining-upward cycle, from conglomerate and breccia at the base to alternating sandstone-mudstone in the depocentre, which interfingers with the fault-scarp facies of the detachment. Sediment dispersal was transverse-dominated and occurred through coalescing alluvial fans from the immediate hanging wall and/or footwall of the detachment. Different stratigraphic sections reveal important lateral facies variations that correlate with major corrugations of the detachment fault. The latter represent extension-parallel folds that formed largely in response to the *ca*. N-S constrictional strain regime of the transtensional plate boundary. The upward vertical deflection associated with antiformal folding dampened subsidence in the northeastern Santa Rosa basin, and resulted in steep topographic gradients with a high influx of coarse conglomerate here. By contrast, the downward motion in the synform hinge resulted in increased subsidence, and led to a southwestward migration of the depocentre with time. Thus, the Santa Rosa basin represents a new type of transtensional rift basin in which oblique extension is partitioned between diffuse constriction and discrete normal faulting. $^{40}Ar/^{39}Ar$ geochronology of intercalated volcanic rocks suggests that transtensional deformation began during the Late Miocene, between 9.36 ± 0.14 Ma and 6.78 ± 0.12 Ma, and confirms previous results from low-temperature thermochronology (Seiler *et al.*, 2011). Two other volcanic units that appear to be part of a conformable syn-rift sequence are, in fact, duplicates of pre-rift volcanics and represent allochthonous, gravity-driven slide blocks that originated from the hanging wall.

INTRODUCTION

Sedimentation in rifted basins is primarily controlled by the geometry, magnitude, rate and deformation history of the basin-bounding fault and the available sediment supply (e.g., Leeder & Gawthorpe, 1987; Gawthorpe & Leeder, 2000). Two end-member models have been invoked to describe the stratigraphy of continental extensional basins. Rift basins are typically asymmetric half-grabens with depocentres that are proximal to the basin-bounding fault and hanging wall-derived sediment influx (Leeder & Gawthorpe, 1987). By comparison, supradetachment basins are dominated by alluvial fans shed from the footwall with depocentres that are removed from the main fault (Friedmann & Burbank, 1995). A number of studies have documented facies distributions that are largely consistent with either the asymmetric rift basin or the supradetachment basin model (e.g., Gupta *et al.*, 1999; Davies *et al.*, 2000; Bosworth *et al.*, 2005; Mack *et al.*, 2006), although not all basins behave according to model predictions (Janecke *et al.*, 1999; Mack & Stout, 2005).

Correspondence: C. Seiler, School of Earth Sciences, The University of Melbourne, Victoria 3010, Australia. E-mail: seilerc@unimelb.edu.au Email addresses: seilerc@unimelb.edu.au (C. Seiler), mark.quigley@canterbury.ac.nz (M.C. Quigley), jfletche@cicese.mx (J.M. Fletcher), dphillip@unimelb.edu.au (D. Phillips), gleadow@unimelb.edu.au (A.J.W. Gleadow), b.kohn@unimelb.edu.au (B.P. Kohn).

Compared with extensional basins, the facies architecture of transtensional basins is more complicated because of the interactions between coeval normal and strike-slip faults, vertical-axis block rotations and syntectonic folding, all of which are likely to affect the subsidence and sedimentation patterns of the basin. Over the past decade, significant progress has been made in understanding the geometry and facies configuration of transtensional basins (e.g., Dorsey & Martin-Barajas, 1999; Osmundsen & Andersen, 2001; Cope *et al.*, 2010; Sözbilir *et al.*, 2011; Dorsey & Umhoefer, 2012). In most instances, sedimentation patterns are primarily controlled by interacting normal and strike-slip faults, and the basins are essentially composites between extensional and pull-apart basins (e.g., Dorsey & Martin-Barajas, 1999; Umhoefer *et al.*, 2007). However, transtensional shear may also be accommodated by distributed constrictional strain that is not localized along fault zones, and clearly more work is needed to characterize the variety of sedimentation patterns that are to be expected in transtensional basins.

The Santa Rosa basin is one of a series of syn-rift basins that developed along the incipient passive margin of northeastern Baja California during oblique rifting in the Gulf Extensional Province (GEP), an area of extended continental crust surrounding the Gulf of California (Fig. 1). Based on detailed structural and kinematic analysis, Seiler *et al.* (2010) demonstrated that the fault array of the Sierra San Felipe, which includes the bounding fault of the Santa Rosa basin (Figs 1b and 2), accommodated transtensional deformation since faulting began during the Late Miocene, sometime after *ca*. 9 Ma (Seiler *et al.*, 2011). This study presents the results of an integrated sedimentological and geochronological study of the pre- and syn-rift stratigraphy of the Santa Rosa basin as an example of a rift basin during transtensional deformation. Using detailed observations from lithofacies distributions, clast point-counts, sedimentary structures and palaeocurrents, we document the sedimentation patterns of the Santa Rosa basin, which are influenced by both extensional faulting and the more subtle effects of transtensional deformation, including strike-slip faulting, vertical-axis block rotations and constrictional folding. These observations are then integrated with $^{40}Ar/^{39}Ar$ geochronology of pre- to syn-rift volcanic rocks to reconstruct in more detail the tectonic evolution of the Santa Rosa basin and detachment, and improve existing timing constraints on deformation.

TECTONIC AND GEOLOGICAL SETTING

The Gulf of California is a young oceanic basin that is currently undergoing the transition from continental rifting to oceanic spreading. Opening of the Gulf of California is the result of transtensional shearing between the Pacific and North American plates (e.g., Atwater, 1970) that began after subduction west of Baja California ceased between *ca*. 12–8 Ma (Mammerickx & Klitgord, 1982; Michaud *et al.*, 2006). Present-day relative plate motion is primarily accommodated by the gulf axis system of nascent spreading centres and transform faults, separating Baja California from North America at a rate of *ca*. 43–47 mm/yr (Plattner *et al.*, 2007). Restorations across the northern Gulf indicate that since *ca*. 6 Ma, the bulk of this highly oblique motion – the angle between the relative plate motion vector (*ca*. 320° after *ca*. 8 Ma [chron 4]; Atwater & Stock, 1998) and the rift trend in this region is *ca*. 20° – occurred localized within Gulf of California (Oskin & Stock, 2003a). Despite extreme stretching (*ca*. 1000%), extensional centres in the northern Gulf are not yet producing magnetically lineated oceanic crust (Klitgord *et al.*, 1974), and crustal thicknesses remain high (>20 km onshore, *ca*. 14–17 km offshore; González-Fernández *et al.*, 2005). Onshore Baja California, extension was significantly less (e.g., *ca*. 10% in the southern Sierra San Felipe) even though most faults of the GEP remained active until the Plio- to Pleistocene (e.g., Stock & Hodges, 1989; Seiler *et al.*, 2010) and many are still active today (e.g., Fletcher & Mungúia, 2000; Fletcher & Spelz, 2009).

Prior to *ca*. 6 Ma, the kinematic evolution of the plate boundary is less well understood. It has long been thought that the transtensional strain of the plate boundary was partitioned into strike-slip faulting west of Baja California and orthogonal extension east of the peninsula (e.g., Stock & Hodges, 1989). However, it has recently emerged that faults west of Baja California accommodated significantly less strike-slip motion than is required by the strain partitioning model (Fletcher *et al.*, 2007), and it now appears likely that rifting in the GEP was oblique-divergent from at least *ca*. 9–8 Ma onward (Seiler *et al.*, 2010, 2011).

The Sierras San Felipe and Santa Rosa comprise a series of fault-bound ranges and basins within the GEP of NE Baja California, Mexico (Fig. 1). The area is separated from the relatively stable portion of the Baja California microplate by the NNW striking San Pedro Mártir fault, an active normal fault with a topographic escarpment of up to 2.5 km that represents the breakaway fault in this segment of the rift (Fig. 1b; Gastil *et al.*, 1975). Although high-angle at the surface, the scalloped trace and differential tilting between foot and hanging wall suggest that the San Pedro Mártir fault is listric (Hamilton, 1971; Dokka & Merriam, 1982), and likely develops into a basal detachment that extends towards the Gulf of California. In this scenario, the Sierras San Felipe and Santa Rosa represent W- to NW-tilted extensional allochthons in the hanging wall of the San Pedro Mártir fault (Fig. 1b). Palaeomagnetic results from the Tuff of San Felipe indicate that the upper plate of the San Pedro Mártir fault underwent significant clockwise vertical axis rotations of between *ca*. 40–70° since *ca*. 12.6 Ma (Fig. 1b; Stock *et al.*, 1999).

The eastern range front of the Sierras San Felipe and Santa Rosa is controlled by a left-stepping *en echelon* array of four moderate- to low-angle normal faults that juxtapose Mesozoic basement in the footwall against syntectonic basin-fill in the hanging wall (Fig. 1b; Stock &

Hodges, 1990; Lewis & Stock, 1998a; Seiler *et al.*, 2010). Deformation between the main fault strands is relayed by three kinematically complex transfer and accommodation zones (Fig. 1b; Seiler *et al.*, 2010).

The Las Cuevitas detachment bounds the northern Sierra San Felipe and accommodates up to *ca*. 9 km of E- to SE-directed displacement (Fig. 1b; Seiler *et al.*, 2010). In its hanging wall, the Llano El Moreno basin is an asymmetric half-graben in which Oligocene(?) to Middle Miocene pre-rift strata are overlain by a fanning sequence of Late Miocene to Pliocene sedimentary rocks (Black, 2004). Low-temperature thermochronology of the Las Cuevitas footwall is consistent with available stratigraphic constraints and suggests that slip on the detachment started at *ca*. 9–8 Ma (Seiler *et al.*, 2011). Subsidence initially outstripped sediment supply and, by the latest Miocene, the basin had deepened from a subaerial alluvial fan environment to deposition of a marine diatomite (Boehm, 1984; Black, 2004). After *ca*. 3.6 Ma, waning to terminal fault slip led to a progressive shoaling of the basin and a return to subaerial conditions (Black, 2004). The southern Llano El Moreno basin is thought to be affected by broadly right-lateral shear in the Cuevitas transfer zone, an inferred relay structure that transfers strain from the Las Cuevitas to the Santa Rosa detachment (Seiler *et al.*, 2010).

The Santa Rosa detachment is a strongly corrugated, NW- to NE-striking fault system that controls the eastern mountain front of the central Sierra San Felipe and Sierra Santa Rosa and exhibits complex variations in both fault orientation and kinematics (Fig. 1b). North of a prominent antiformal fault corrugation, the fault system is dominated by steeply dipping dextral-oblique faults with subordinate ENE- to SE-directed moderate- to low-angle normal faulting (Fig. 1b; Seiler *et al.*, 2010). Northward decreasing fault slip and the dominant strike-slip kinematics resulted in only minor hanging wall subsidence and prevented the development of a major syntectonic basin here (Fig. 1b). Near the hinge of the antiformal corrugation, the fault splays into two separate strands (Seiler *et al.*, 2010): the Amarillo fault continues along the SE Sierra Santa Rosa and develops along-strike into the sinistral-reverse Amarillas transfer zone (Figs 1b and 2). The Santa Rosa detachment *s.str.* bends sharply southwestward and develops into a shallowly SE-dipping low-angle normal fault (<30°) that controls the NW margin of the Santa Rosa basin (Figs 1b and 2). This detachment splay accommodated between *ca*. 3.8 and 5.2 km of SE-directed dip-slip movement and shows only minor oblique-slip deformation (Seiler *et al.*, 2010). Cut-off angles decrease from *ca*. 55–60° in pre-rift strata to *ca*. 40° further upsection, indicating that the detachment initiated as a high-angle normal fault and rotated progressively during fault slip (Seiler *et al.*, 2010). Towards its southern end, the Santa Rosa detachment enters a broad synformal domain before it abuts on the dextral western section of the Amarillas transfer zone, which changes to sinistral further east (Figs 1b and 2). Modelling of apatite fission track and (U-Th)/He data from the detachment footwall suggests that faulting began at *ca*. 9–7 Ma (Seiler *et al.*, 2011).

Overlying the NW-tilted Sierra Santa Rosa, the Santa Rosa basin is located in the hanging wall of the Santa Rosa detachment SW of the major antiformal corrugation (Figs 1b and 2). The basin is well-exposed due to its location in the footwall of the Amarillo fault and comprises an intercalated sequence of Miocene to Pleistocene sedimentary and volcanic units (Fig. 2; Bryant, 1986). Pre-rift strata are Early to Middle Miocene in age and dip N to W into the detachment. Bedding dips decrease from *ca*. 50–60° in the NE to much shallower angles of *ca*. 30–40° in the southwestern basin (Fig. 2; Seiler *et al.*, 2010). A similar change in dip angle does not appear to affect the youngest syn-rift strata (Fig. 2). Combined with marginally steeper detachment dips in the SW, this suggests that crustal levels exposed in the northeastern Santa Rosa basin are structurally deeper than those in the SW basin. The syn-rift sequence consists of interbedded conglomerate, sandstone and mudstone that have previously been interpreted as alluvial fan and floodplain deposits (Bryant, 1986). The basin-fill defines an overall fining-up trend that culminates in playa-lacustrine deposition and develops into an upward coarsening sequence further towards the detachment fault (Seiler *et al.*, 2010). Intercalated within these sediments are three volcanic units with K/Ar ages that are not consistent with their stratigraphic level (Gastil *et al.*, 1979; Bryant, 1986). The syntectonic basin fill is unconformably overlain by Quaternary alluvial fans that post-date movement on the detachment (Seiler *et al.*, 2010).

South of the Amarillas transfer zone, the N-S striking Huatamote detachment is a dip-slip low-angle normal fault with *ca*. 4.5 km of ESE-directed displacement (Figs 1b and 2; Seiler *et al.*, 2010). The Huatamote basin

Fig. 1. a) Location map and regional tectonic setting of northwestern Mexico showing the main tectonic features of the transtensional plate boundary in the Gulf of California. b) Geological map of the Sierra San Felipe in northeastern Baja California (simplified from Andersen, 1973; Gastil *et al.*, 1975; Lewis & Stock, 1998a; Stock, 2000; Oskin, 2002; Black, 2004; Seiler, 2009). The Sierra San Felipe consists of a series of W- to NW-tilted extensional allochthons in the hanging wall of the San Pedro Mártir fault, the break-away fault for rifting. The eastern range front of the Sierra San Felipe is defined by an en echelon array of four moderate to low-angle normal faults/detachments that are interconnected by transfer faults and accommodation zones. Palaeomagnetic declination anomalies are relative to a reference location (ref) in the southern Sierra San Felipe (data from Lewis & Stock, 1998b; Stock *et al.*, 1999). ATZ=Amarillas transfer zone, CTZ=Cuevitas transfer zone, HAZ=Huatamote accommodation zone, Hb=Huatamote basin, HD=Huatamote detachment, GEP=Gulf Extensional Province, LCD=Las Cuevitas detachment, LMb=Llano El Moreno basin, PVP=Puertecitos Volcanic Province, SRb=Santa Rosa basin, SRD=Santa Rosa detachment.

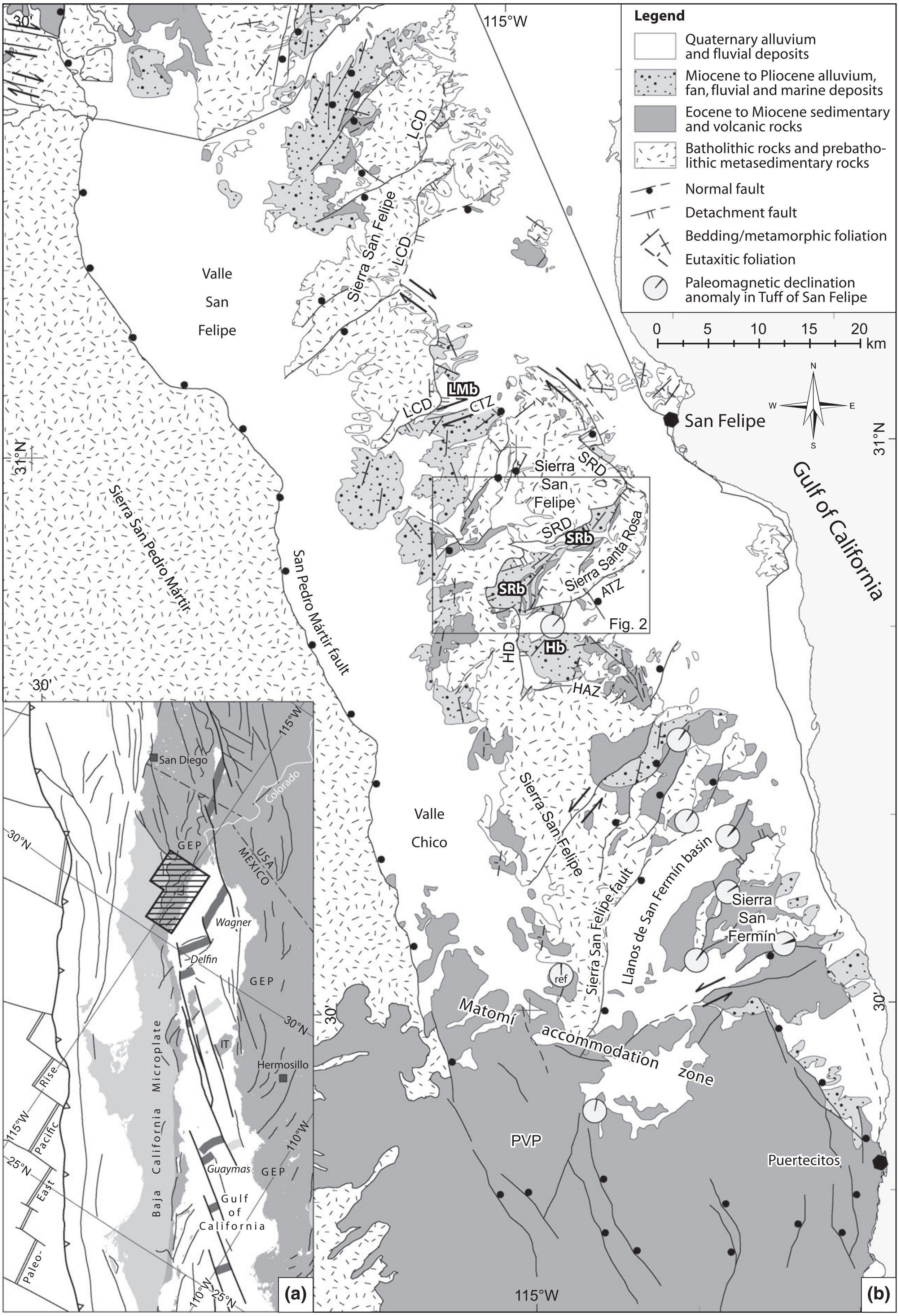
Legend
Quaternary alluvium and fluvial deposits
Miocene to Pliocene alluvium, fan, fluvial and marine deposits
Eocene to Miocene sedimentary and volcanic rocks
Batholithic rocks and prebatholithic metasedimentary rocks
Normal fault
Detachment fault
Bedding/metamorphic foliation
Eutaxitic foliation
Paleomagnetic declination anomaly in Tuff of San Felipe
0 5 10 15 20 km
N
W
E
S
115°W
30'
31°N
Valle San Felipe
Sierra San Felipe
LCD
LMb
CTZ
SRD
Sierra San Felipe
SRb
Sierra Santa Rosa
ATZ
Fig. 2
HD
Hb
HAZ
San Felipe
Gulf of California
Sierra San Pedro Mártir
San Pedro Mártir fault
Valle Chico
Sierra San Felipe
Sierra San Felipe fault
Llanos de San Fermín basin
Sierra San Fermín
ref
Matomí accommodation zone
PVP
Puertecitos
(a)
(b)
San Diego
Colorado
GEP
USA
MEXICO
Wagner
Delfín
30°N
IT
Hermosillo
110°W
Guaymas
Gulf of California
Baja California Microplate
Paleo- East Pacific Rise
25°N

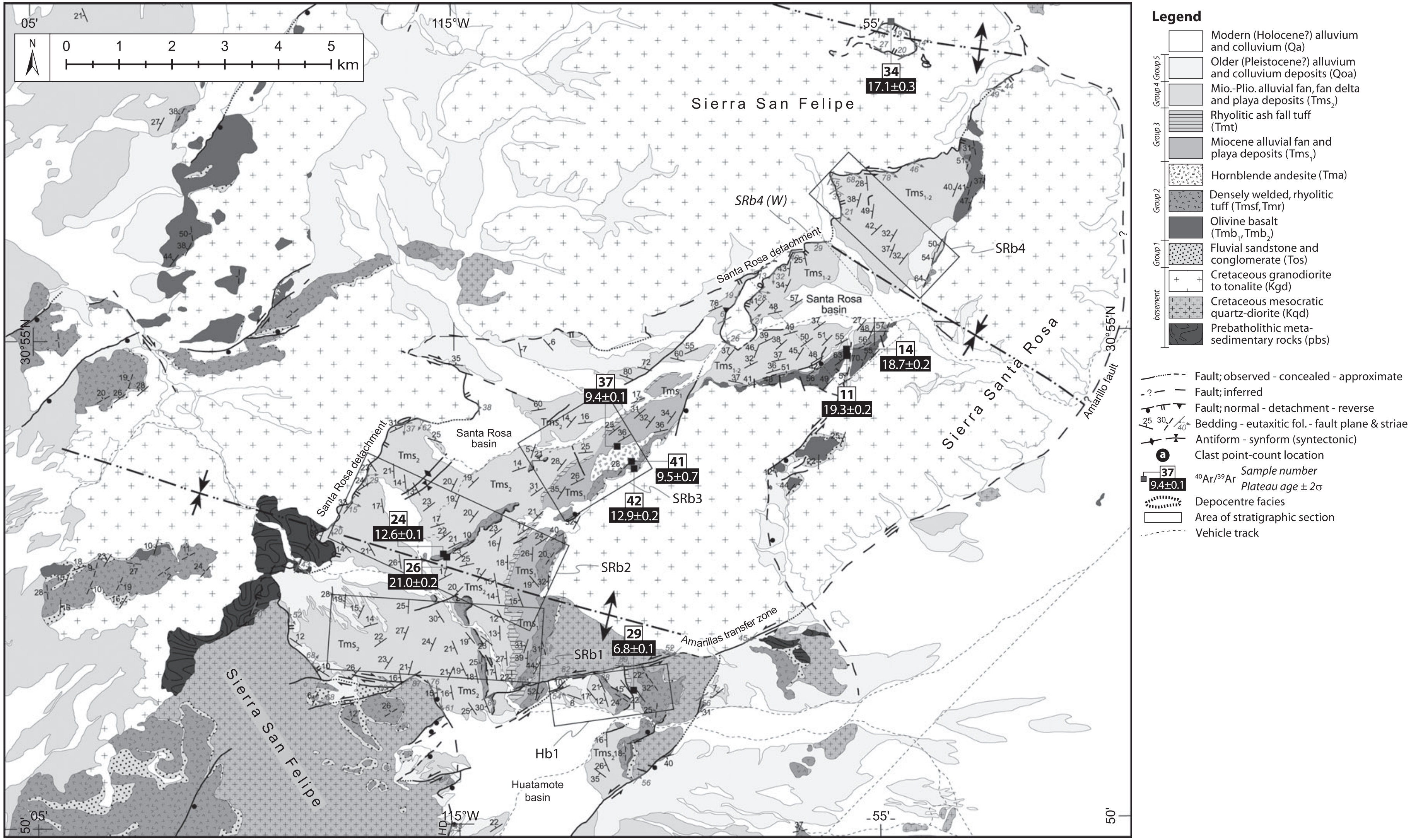

Fig. 2. Geological map of the Santa Rosa basin and surrounding areas (after Bryant, 1986; this study). Rectangles show the location of stratigraphic sections. The syn-rift stratigraphy comprises a Late Miocene to Pleistocene sequence of intercalated sedimentary and volcanic rocks that dip NW into the detachment fault. Both the detachment (double-dotted dashed lines) and the basin-fill (single-dotted dashed lines) have been folded as part of the N-S constrictional strain regime of the transtensional plate boundary. See Fig. 1 for location. SRb1 = Santa Rosa basin section 1, SRb2 = Santa Rosa basin section 2, SRb3 = Santa Rosa basin section 3, SRb4 = Santa Rosa basin section 4, SRb4(W)=Informal section west of SRb4 where detailed orientation measurements are available for the purpose of Fig. 9, Hb1 = Huatamote basin section 1.

in its hanging wall has not been studied in detail but likely contains similar Miocene to Pleistocene alluvial fan deposits as the Santa Rosa basin (Fig. 1b). Unlike the latter, the Huatamote basin is dissected into at least three to four major fault-blocks (Fig. 1b). Slip on the Huatamote detachment post-dates the *ca*. 12.6 Ma Tuff of San Felipe, but there are no syntectonic volcanic or marine rocks that could be used to refine its age. Towards the southern tip of the detachment, right-lateral shear in the Huatamote accommodation zone relays deformation SE onto the Sierra San Felipe fault (Fig. 1b; Seiler *et al.*, 2010). The latter marks the SE edge of the southern Sierra San Felipe and shows *ca*. 700 m of ESE-directed normal displacement that started between *ca*. 12.6 and 6 Ma (Stock & Hodges, 1990; Lewis & Stock, 1998a). The Llano de San Fermín basin in its hanging wall is mostly buried beneath Quaternary alluvium but may be dissected by several NW-dipping normal faults (Lewis & Stock, 1998a).

STRATIGRAPHY

The stratigraphy of the Santa Rosa basin as described below is based on geological mapping of the study area and a series of five detailed stratigraphic sections (Hb1, SRb1, SRb2, SRb3, SRb4), collected to characterize both vertical and lateral facies patterns over time. Simplified stratigraphic sections are shown in Fig. 3 (detailed sections available as supplementary Fig. S1), with section locations and clast point-count localities shown in Figs 2 and 5 respectively.

The stratigraphy of the Santa Rosa basin can informally be subdivided into five main groups above the crystalline basement (Fig. 2). These groups are broadly similar to the stratigraphic framework of the southern Sierra San Felipe (Stock, 1989; Lewis, 1996; Oskin & Stock, 2003b), although differences exist in late pre- to syn-rift rocks. Group 1 deposits represent a thin, discontinuous veneer of Oligocene to Early Miocene fluvial sandstone and conglomerate that lie nonconformably above the Mesozoic basement (Figs 2–4a; Table 1). Group 2 consists of basaltic to andesitic lava flows of the Miocene volcanic arc and a rhyolitic ignimbrite, the Tuff of San Felipe (cf. Stock *et al.*, 1999; Figs 2 and 3; Table 1). Groups 3 and 4 encompass the syntectonic basin-fill of the Santa Rosa basin and comprise a sequence of sediments and intercalated volcanic rocks that are capped in an angular unconformity by post-tectonic conglomerate of group 5 (Figs 2 and 3). Detailed lithological descriptions of pre-rift deposits are listed in Table 1, syn-rift strata are described below.

Late Miocene syn-rift deposits (group 3)

Lower syn-rift sediments (Tms_1)

Late Miocene syntectonic deposits (Tms_1) are dominated by conglomerate and interbedded conglomerate-sandstone that interfinger laterally with less voluminous breccia and sandstone-mudstone sequences. The full stratigraphic section of Tms_1 is up to *ca*. 200 m thick and is exposed in the central Santa Rosa basin (stratigraphic level of between *ca*. 100–160 m and 340 m in SRb3; Fig. 3d). The base of Tms_1 is formed by a discontinuous monolithologic megabreccia that is up to *ca*. 90 m thick and lies depositionally above an andesite flow of group 2 (SRb3; Fig. 3d; Bryant, 1986). The megabreccia is laterally discontinuous and only outcrops in the central part of the basin (SRb3; Fig. 3d). The clast-supported megabreccia is unstratified and contains pebble- to boulder-sized (up to several metres) clasts of very angular to subangular granodiorite (Fig. 4b). The tan-brown matrix consists of very poorly sorted quartzofeldspathic sand.

The megabreccia is overlain by pebble-cobble conglomerate that is partially interbedded with sandstone and that forms the base of the section where the megabreccia is missing (Figs 3c–e and 4c). Conglomerates are matrix- to clast-supported (5–70%) and moderately to very poorly sorted (Fig. 4c). Clasts are angular to rounded and range in size from granules to boulders (mean of 10–30 cm) in a tan-brown matrix of medium-coarse, immature arkosic sand (Fig. 4c). Stratification is poorly to well developed and consists of tabular to broadly lenticular beds of *ca*. 5–50 cm thickness. Beds sometimes show clast imbrications and may be truncated by channels. Average and maximum clast sizes decrease upsection and sandy beds become increasingly common (Fig. 3d). Sandstone beds consist of arkosic medium sand that is tan-brown in colour, well sorted and exhibits thin laminar to cross-bedded stratification. Further upsection, conglomerate beds become increasingly rare, although channels are still present (Fig. 3d). Here, the dominant lithofacies is sandstone, which occurs in <1 m thick beds of moderately sorted sandstone with rare pebble clasts. Stratigraphically higher, sedimentation becomes dominated by alternating sandstone and red-brown mudstone, thus defining an overall fining-up sequence (Figs 3d and 4d). Foresets capped by symmetric ripples and mudcracks suggest an ephermal depositional environment (Figs 3d and 4e–f).

Further NE and SW (SRb2, SRb4), deposits are dominated entirely by pebble-cobble conglomerate similar to the one described above (Fig. 3c,e). In section SRb2, the conglomerate shows a subtle fining-up trend defined by a slight decrease in average clast size and increasing abundance of (rare) sandstone beds (Fig. 3c). By contrast, SRb4 records an upward increase in the average clast size (Fig. 3e). In SRb4, a *ca*. 5–10° angular unconformity within the lowest group 3 deposits suggests that tilting of the hanging wall and therefore faulting on the detachment occurred synchronously with deposition of group 3 strata (Fig. 3e). Note that some of the above observations were made adjacent to section SRb4, as the lower part of the section there is covered by Quaternary alluvium.

The coarse lithofacies of the lower group 3 strata in the central and NE Santa Rosa basin interfingers laterally with fine grained sandstone and sandstone-mudstone of

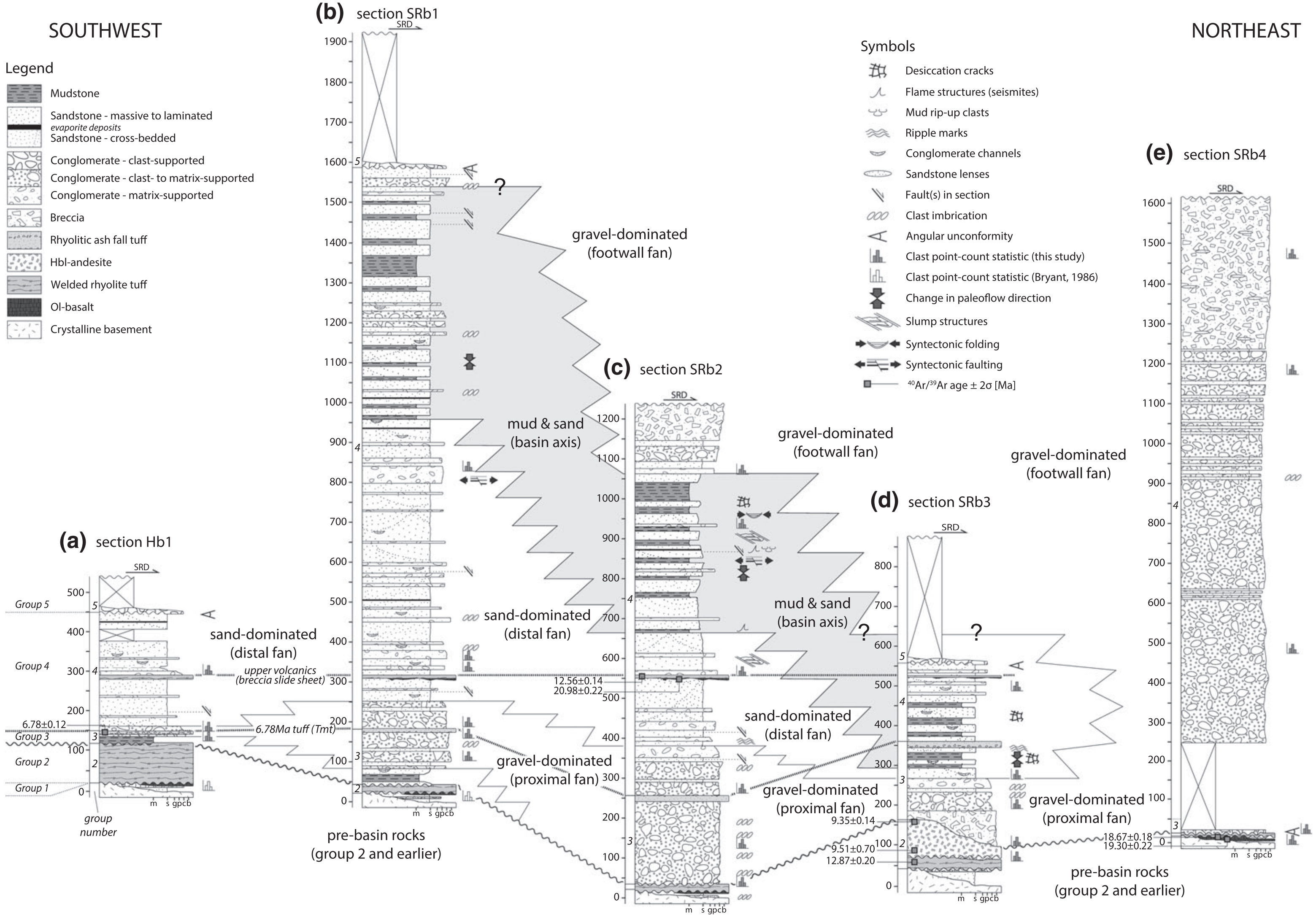

Fig. 3. Simplified stratigraphic sections of the Santa Rosa basin. Sections are arranged according to their position in the basin from southwest (left) to northeast (right). Reported stratigraphic thicknesses are based on a combination of (1) tape measurements in the field, (2) estimated thickness in the field (group 1 & 2 strata only), (3) reported stratigraphic thickness from Bryant (1986), and (4) trigonometric calculation based on GPS locations and a barometric altimeter, and the average orientation of strata between adjacent GPS locations. Due to limitations that are inherent to any syntectonic half-graben (e.g. internal faulting, down-dip thickening of strata in a sedimentary wedge, uniform tilting towards the basin-bounding fault that makes discerning temporal from across-strike spatial variations nearly impossible), thicknesses should be considered approximate only. Realistic errors in reported thickness values between measurements are probably in the order of a few metres to tens of metres and do not change the key points of our interpretation. Refer to Fig. 2 for section locations and supplementary Fig. S1 for detailed stratigraphic sections.

Table 1. Description of pre-rift lithologies

Lithology	Description
Basement	
Pre-batholithic metamorphic rocks (pbs)	Psammopelitic schists and quartzites exposed in footwall of southern Santa Rosa detachment (Fig. 2). Greenschist to amphibolite facies metamorphism (Rothstein & Manning, 2003). Exposures of marble, slate, amphibolite and chert to the northeast and south of the study area. *Age:* Neoproterozoic(?) to Jurassic (Anderson, 1993)
Plutonic rocks (Kgd, Kqd)	Cretaceous magmatic arc, part of the Peninsular Ranges batholith (see also, e.g., Gastil *et al.*, 1975). Crosscut by <50 cm wide (hornblende-biotite) pegmatite and aplite dikes. Local evidence for magma mingling (fine-grained mafic enclaves). *Granodiorite (Kgd)*: leucocratic biotite-hornblende granodiorite and tonalite. Fine- to coarse-grained, unfoliated with rare magmatic layering. Dominant intrusive north of the Amarillas transfer zone (Fig. 2). *Quartz-diorite (Kqd)*: meso- to melanocratic biotite-hornblende quartz-diorite. Fine- to medium-grained, partially foliated with some magmatic layering. Contact to granodiorite is intrusive (rarely faulted). Exposed in southern study area, dominant intrusive south of the Amarillas transfer zone (Fig. 2). *Age:* Late Cretacous (*ca.* 99–92 Ma; Kimbrough *et al.*, 2001)
Group 1	
Sandstone and conglomerate (Tos)	Moderately indurated arkosic sandstone with minor conglomerate beds and channels (Fig. 4a; see also, e.g., Dorsey & Burns, 1994; Oskin & Stock, 2003a). Nonconformably overlies basement in gently undulating palaeosurface with E–W drainages. *Thickness*: <35 m, discontinuous. *Sandstone:* immature, medium to coarse sand, moderately to well sorted. Buff to red-, orange-brown in colour, red baked at contact with group 2 volcanics. Indistinct to thin tabular bedding (typically <1 cm) with some internal fining upward cycles. In southwestern Santa Rosa basin contains a discontinuous lens of tabular bedded limestone (<1 m thick). *Conglomerate:* matrix-supported with granule- to cobble-sized, angular to well-rounded clasts, very poorly sorted. Mixed clast assemblages: plutonic ± metamorphic ± volcanic ± sedimentary ± carbonate. Provenance: local & exotic (i.e., fossil-bearing limestone from Sonora (Gastil *et al.*, 1973), exotic volcanic agglomerate). SW- to NW-directed palaeotransport (clast imbrications; Fig. 4a). *Depositional environment:* fluvial (locally: lacustrine, eolian). *Age:* Oligocene to earliest Miocene (32–21 Ma, bracketed by apatite fission track basement ages and $^{40}Ar/^{39}Ar$ of group 2 volcanics; Seiler *et al.*, 2011; this study)
Group 2	
Olivine basalt (Tmb_1)	(Dark) grey to grey-brown basalt flows overlying basal sediments or basement. *Thickness:* 5–20 m (SW) to *ca.* 100 m (NE), discontinuous. Aphanitic to vesicular or amygdaloidal texture with up to 10% yellow to red-brown olivine phenocrysts (<2 mm), variably altered to iddingsite. Individual flows often have an autobrecciated base and/or a <1 m thick basal unit of red, red-brown, purple-red vesicular basalt or scoria with veins of secondary calcite. Elongated vesicles indicate vent to east or west of Santa Rosa basin. *Thin section:* pilotaxitic matrix of plagioclase + pyroxene + iron oxide (plus secondary chlorite, mica and calcite) containing phenocrysts of olivine ± plagioclase ± pyroxene. *Age:* Early to Middle Miocene (21–15 Ma; Gastil *et al.*, 1979; this study)

(continued)

Table 1 (*continued*)

Lithology	Description
Tuff of San Felipe (Tmsf)	Regionally extensive pyroclastic flow deposit (see also, e.g., Stock *et al.*, 1999; Oskin & Stock, 2003b). Disconformably overlies older lithologies, useful pre-rift marker horizon. *Thickness: ca.* 10–30 m (up to *ca.* 100 m in palaeotopographic low in northern Huatamote basin). Pink, purple(-grey), orange- or red-brown ignimbrite with up to 10% lithics of basalt and rhyolite. Well-developed eutaxitic foliation defined by pumice fiammes (typically *ca.* 10%). Black vitrophyre (<1–1.5 m thick) at base is locally underlain by weakly to moderately welded, lithic-rich brown tuff and (rarely) nonwelded, pinkish white ash fall tuff. Lower orange-red spherulitic horizon (2–3 m thick) develops into thick section of densely welded and strongly indurated ignimbrite. Upper contact is erosional (channel incision and nonwelded top missing). Vent location east of Isla Tiburón (Oskin & Stock, 2003b). *Thin section:* devitrified quartz-feldspar matrix with ~5–15% phenocrysts (sanidine $\gg$ hornblende $\approx$ quartz $\approx$ biotite). *Age:* Middle Miocene (*ca.* 12.6 Ma; Stock *et al.*, 1999; this study)
Hornblende andesite (Tma)	Orange- to pale olive-grey andesite flow. *Thickness:* <90 m, local occurrence in central Santa Rosa basin. Aphanitic groundmass with *ca.* 5–10% phenocrysts of columnar to acicular hornblende $\gg$ plagioclase. Directly overlies Tmsf (rarely Tmvc). *Thin section:* fine-grained matrix of plagioclase + amphibole + opaques, secondary calcite in cracks. *Age:* Late Miocene (9.36 Ma; Bryant, 1986; this study)
Sandstone and conglomerate (Tmvc)	Siliciclastic to volcaniclastic sandstone and conglomerate. *Thickness:* <5–10 m, discontinuous lenses in various stratigraphic positions within group 2 volcanics. *Within Tmb1:* red-brown, moderately to very well sorted arkosic sandstone; incised by conglomerate palaeochannels. *Tmb1-Tmsf-Tma:* volcaniclastic pebble to cobble conglomerate in palaeochannels between volcanic units (rare), clasts derived from immediately underlying volcanic rocks. *Depositional environment:* fluvial, erosion-dominated. *Age:* Early to Late Miocene (21–9 Ma; this study)

the SW basin (Hb1, SRb1; Fig. 3a and b). This facies change is associated with a strong gradient in stratigraphic thickness, which decreases from *ca*. 200 m in the central basin (SRb2, SRb3) to <25 m south of the Amarillas transfer zone (Hb1) before pinching out altogether further south (Fig. 3a–d). Immediately north of the Amarillas transfer zone (SRb1; Fig. 3b), the oldest sediments consist of poorly indurated, tan to red-brown sandstone that is poorly to moderately sorted, moderately mature, medium to coarse grained and contains *ca*. 10% granules. The sandstone fines upsection into a *ca*. 18m thick section of interbedded sandstone-mudstone (SRb1, Fig. 3b). Bed thickness ranges between *ca*. 2–20 cm (mudstone) and *ca*. 30 cm (sandstone). Further upsection, group 3 records a coarsening-up cycle to sandstone-conglomerate (the latter is increasingly dominant) that is very similar to the sandstone-conglomerate sequence of the central Santa Rosa basin (Fig. 3b–d). South of the Amarillas transfer zone (Hb1, Fig. 3a), the lower group 3 sandstone-mudstone facies directly overlies the Tuff of San Felipe and lacks the coarsening-up trend seen further NE. Instead, the fine-grained facies is truncated by a *ca*. 2.2 m thick clast-supported cobble conglomerate that contains granule-to boulder-sized clasts of welded tuff $\gg$ granodiorite $\approx$ olivine basalt (Fig. 3a).

Interpretation: The megabreccia at the base of group 3 in the central Santa Rosa basin (SRb3) are interpreted as sediment-gravity flows deposited in the piedmont zone of proximal alluvial fans (e.g., Bull, 1972, 1977; Blair & McPherson, 1994), most probably as rock falls or rock avalanches originating from the developing escarpment of the Santa Rosa detachment. The megabreccia is laterally equivalent to the sandstone-mudstone facies of the SW Santa Rosa basin (SRb1-2), which probably accumulated during lacustrine(?) suspension sedimentation in a pre-tectonic depression near the present-day location of the Amarillas transfer zone. The fining-up sequence of conglomerate through to sandstone corresponds to progressively more evolved intermediate to distal alluvial fans, where deposition was dominated by sheetflood events. Upsection (basin-ward) decreasing clast sizes in SRb3 indicate a transition to an even more distal alluvial fan environment, in which back-filled palaeochannels facilitate the transport of coarser grained detritus to the distal fan. Occasional outsized clasts (up to boulder) within the finer-grained facies are probably reworked from earlier syn-rift deposits during large discharge events. Near the top of group 3 in SRb3, alternating sandstone and mudstone interbeds represent fine grained sedimentation in fan deltas grading into playa deposits of the depocentre, which is defined by both the fine-grained basin-axis facies and a change in palaeoflow directions (see below).

Rhyolitic ash fall tuff (Tmt)

A nonwelded ash fall tuff (Tmt) caps group 3 sediments in the SW part of the Santa Rosa basin (Figs 2 and 3a–d). The rhyolite tuff is typically buff in colour and contains *ca*. 5–10% phenocrysts of sanidine $\gg$ biotite ± quartz ± amphibole ± muscovite. Thin section analysis revealed sanidine + quartz + hornblende + biotite ± plagioclase ± muscovite in a devitrified glass shard matrix with secondary calcite in cracks. Tmt contains $\leq 20\%$ lithic fragments that are < 5 cm in diameter and consist almost exclusively of welded rhyolite (presumably Tuff of San Felipe). In places, the basal contact comprises a *ca*. 15 cm thick zone with up to *ca*. 60% lithics. The tuff is *ca*. 15 m thick in the central Santa Rosa basin, where a buff lower unit is overlain by a second, pale pink layer with slightly less lithic fragments. Along-strike, Tmt thins in either direction until it is covered by modern alluvium (NE) or pinches out (SW; Figs 2 and 3a–d). The tuff has previously been dated at 16.6 ± 1.3 Ma (K-Ar whole rock; Bryant, 1986), which is inconsistent with its stratigraphic level above the Tuff of San Felipe (ca. 12.6 Ma; Stock *et al.*, 1999).

Late Miocene to Pliocene syn-rift deposits (group 4)

Upper syn-rift sediments (Tms$_2$)

Group 4 consists of Late Miocene to Pliocene conglomerate, sandstone and sandstone-mudstone (Tms$_2$) that overlie group 3 strata (Figs 2 and 3). Facies assemblages are continuous with Tms$_1$, although there are substantial along-strike variations (Fig. 3). In the central Santa Rosa basin (SRb3), the base of Tms$_2$ is similar to the top of Tms$_1$ and consists of moderately to well sorted, tan arkosic sandstone interbedded with thin, red-brown mudstone (Figs 3d and 4d). Sandstone beds are typically <1 m thick, massive to cross-bedded and contain occasional conglomerate channels and mudcracks (Figs 3d and 4d–f). Upsection, mudstone beds are increasingly rare and are replaced by beds of matrix-supported pebble conglomerate with angular to subangular clasts that are up to boulder-sized (Fig. 3d). This sequence is unconformably overlain by poorly indurated conglomerate of group 5 (Figs 3d and 4d).

In the NE basin (SRb4), Tms$_2$ consists of pebble-cobble conglomerate grading into breccia with minor interbedded sandstone (Fig. 3e). Conglomerates are matrix- to clast-supported (granule to boulder) with a matrix of (very) poorly sorted, tan arkosic sand. Lower group 4 conglomerates typically comprise angular to subrounded pebbles, with clast abundance, size and angularity all increasing upsection (Fig. 3e). Sandstone beds are tabular to laminar stratified, typically *ca*. 15 cm thick and consist of tan- to red-brown, coarse arkosic sand; they are poorly to moderately sorted but become progressively more mature and better sorted upsection. Upsection and towards the Santa Rosa detachment, the conglomerate grades into a megabreccia with very angular cobble- to boulder-grade clasts (<5 m) in a granodiorite-derived matrix of very poorly sorted coarse sand (Fig. 3e). Within the megabreccia are pockets of thinly bedded, well sorted, red-brown sandstone (Fig 3e).

In the SW Santa Rosa basin (SRb1, SRb2), group 4 sediments exhibit a fining-up trend from conglomerate through to sandy mudstone (Figs 3b,c, and 4d). Near the base of Tms_2, conglomerate beds are matrix- to clast-supported with angular to subrounded clasts of pebble to cobble size embedded in (very) poorly sorted, medium-coarse arkosic sand (Figs 3b,c, and 4c). Beds are typically *ca*. 5–20 cm (<2 m) thick and may show graded bedding and clast imbrications. Clast abundance, angularity and size decrease upsection, although large variations exist between beds (Fig. 3b and c). Within the conglomerate are finely laminated to massive sandstone interbeds (*ca*. 0.05–1 m thick) that consist of immature, tan- to red-brown arkosic sand and are moderately to well sorted with rare pebble- to boulder-sized clasts (Fig. 3b and c). Sandstone is rare at the base but is increasingly dominant upsection as conglomerate beds become matrix-supported and less frequent (Fig. 3b and c). Here, sandstone is commonly cross-bedded and contains ripple marks, slumps and flame structures or seismites (Figs 3b,c and 4f). Upsection, sandstones are progressively finer grained, richer in clay minerals and increasingly interbedded with red-brown mudstone, although sorting remains moderate (Figs 3b,c and 4d). Beds are between 2–10 cm (mudstone) and 5–30 cm (sandstone) thick with laminar, massive or cross-bedded stratification (Fig. 4d). Sedimentary structures include slumps, mud rip-ups, mudcracks, asymmetric flame structures (seismites), growth faults and syndepositional folds, which represent either fault-bend folds or fault-propagation folds (Figs 2, 3c and 4e). Further towards the detachment, the fine grained facies interfingers with sandstone-conglomerate and conglomerate in a rapid coarsening-up cycle culminating in boulder conglomerate and megabreccia adjacent to the fault (SRb2; Fig. 3c).

South of the Amarillas transfer zone, the stratigraphy is broadly similar (albeit more condensed) than further NE (Hb1; Fig. 3a). At the base of Tms_2, the conglomerate is significantly thinner and is soon replaced by massive to cross-bedded sandstone with rare conglomerate beds. The section here contains less mudstone beds than elsewhere in the Santa Rosa basin, and both the sandstone-mudstone facies as well as the coarsening-up cycle towards the basin-bounding fault are not developed (Hb1; Fig. 3a).

Interpretation: The depositional environment of group 4 is essentially continuous with that of group 3. The depocentre previously established in SRb3 continued to accumulate fine-grained strata in a distal fan to playa environment, while the southwestern Santa Rosa basin (SRb1-2) now shows a similar retrogradational fining-up trend as earlier seen in SRb3. Within the distal fan facies, sedimentary structures such as slumping or asymmetric seismites suggest deposition on a slightly basin-ward tilted slope during sheetflood events, suggesting that tilting was coeval with deposition. Closer to the detachment, the distal fan to playa facies of the depocentre is laterally intertonguing with an upward coarsening sequence of sandstone, sandstone-conglomerate and conglomerate that represents prograding footwall alluvial fans formed by sheetflood and debris-flow events. The megabreccia that is commonly found near the detachment accumulated as rock fall, rock avalanche and debris-flow deposits in steep alluvial fans shed from the footwall of the Santa Rosa detachment. The asymmetric location of the depocentre (closer to the footwall) with respect to the basin axis probably coincided with the area of most rapid tectonic subsidence and explains the steeper gradient and smaller run-out of alluvial fans from the footwall. Unlike other parts of the basin, the northeastern Santa Rosa basin is entirely dominated by conglomerate and breccia of the proximal fan.

Upper basalt and welded tuff (Tmb_2, Tmr)

In the central and southwestern Santa Rosa basin, lower group 4 strata include a couplet of two intercalated volcanic units: 1) a discontinuous, <5–8 m thick olivine basalt (Tmb_2), overlain by 2) a cliff-forming, densely welded rhyolite tuff of *ca*. 8 m thickness (Tmr; Figs 2–4g). Both units are commonly brecciated with fragments that are very similar in appearance to the Late Miocene basalt (Tmb1) and the Tuff of San Felipe (Tmsf), respectively (cf. Table 1). The upper basalt consists of (dark) grey, granule- to boulder-sized clasts in a light grey to orange-brown matrix (Fig. 4g). Intact clasts are aphanitic to amygdaloidal and contain phenocrysts of red-brown olivine (variably altered to iddingsite) in a pilotaxitic groundmass of plagioclase + pyroxene + iron oxides and secondary chlorite, mica and calcite. Unlike other depositional contacts in group 4, the base of Tmb_2 is highly irregular (Figs 3b–d and 4g). K-Ar dating (plagioclase) of the upper basalt suggests an age of 8.9 ± 1.2 Ma (Gastil *et al.*, 1979).

The upper welded tuff is red-brown to purple-grey in colour and consists of up to *ca*. 15% sanidine phenocrysts in a devitrified glass shard matrix with lithics of basalt > rhyolite. The rhyolitic tuff is densely welded, of probable ash flow origin and contains spherulites and/or pumice fiammes forming a moderately- to well-developed eutaxitic foliation. This foliation is entirely inconsistent across different clasts in brecciated sections, implying substantial post-welding fragmentation. The base of Tmr locally includes thin lenses of vitrophyre (Bryant, 1986). Whole-rock K-Ar dating of the vitrophyre and the tuff yielded ages of 13.6 ± 2.4 Ma and 12.3 ± 1.8 Ma respectively (Bryant, 1986).

Post-tectonic sedimentary strata (group 5)

A thin veneer of moderately to poorly indurated cobble conglomerate (Qoa) overlies older strata in an angular unconformity (Figs 2–4d). The conglomerate is matrix- or clast-supported and consists of locally derived, angular

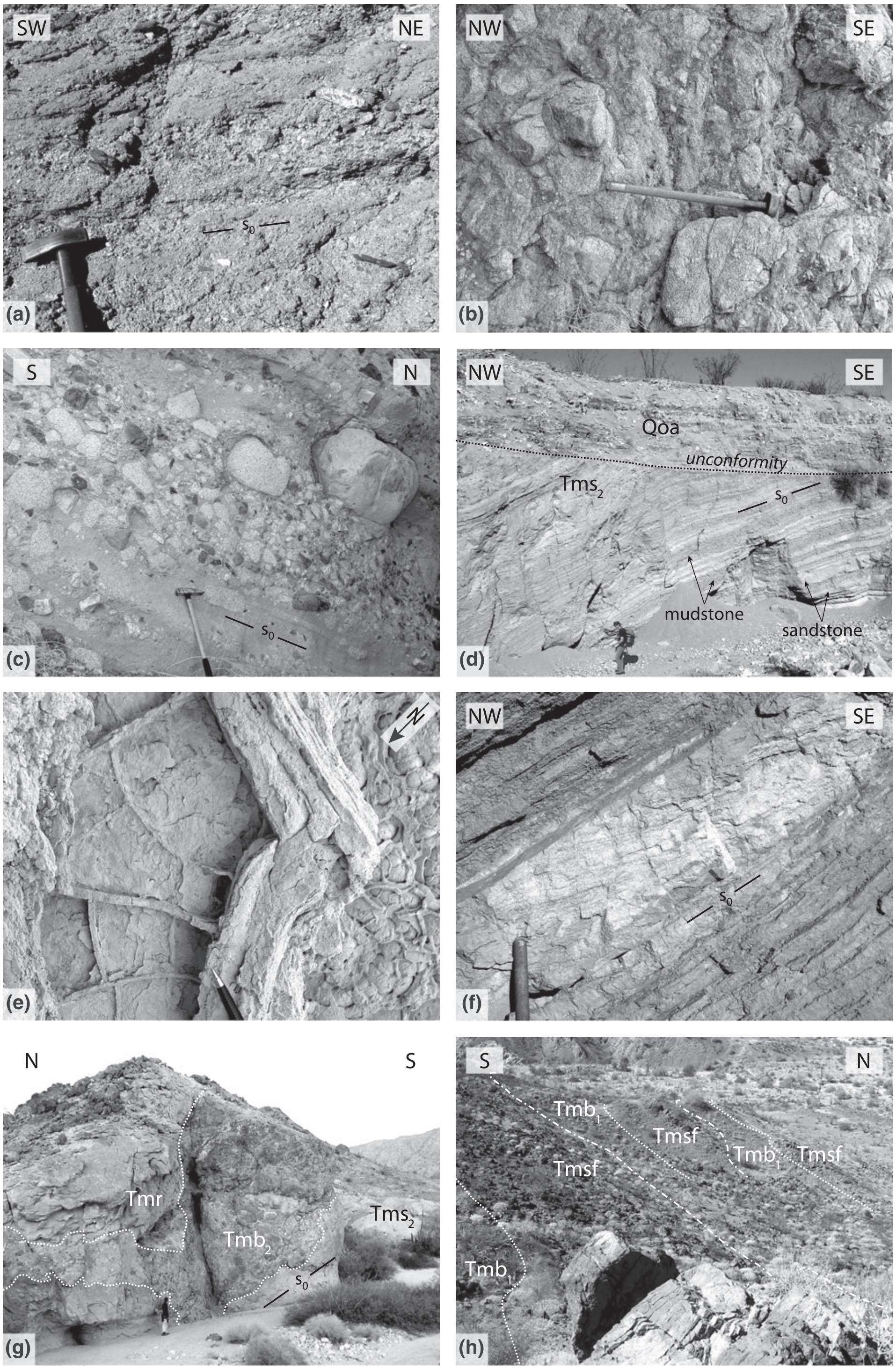

Fig. 4. Field photographs showing: a) Group 1 (pre-rift) fluvial sandstone and conglomerate (Tos) with clast imbrications indicating a palaeoflow direction to the SW. b) Monolithologic megabreccia at the base of Tms_1 in the central Santa Rosa basin that records the onset of rifting. c) Typical syn-rift cobble to boulder conglomerate interbedded with minor sandstone deposits. d) Typical depocentre facies consisting of *ca*. 2–10 cm thick mudstone units interbedded with *ca*. 5–30 cm thick sandstone beds. The depocentre facies is unconformably overlain by subhorizontal Quaternary conglomerate beds that post-date faulting on the detachment. e) Mudcracks within depocentre facies. f) Sandstone bed with ripple marks and foresets within depocentre facies. g) The upper basalt (Tmb_2) and rhyolite tuff (Tmr) of group 4 are duplicates of group 2 volcanics and are thought to have been emplaced as a gravity-driven slide block. Note the highly irregular contact between the underlying sandstone (Tms_2) and the basalt (Tmb_2). h) Small-scale example of two separate slide blocks that triplicate group 2 volcanics in the eastern Santa Rosa basin. Dashed lines show unit boundaries; dash-dotted lines depict interpreted sliding planes.

to subrounded granules to boulders. The tan to red-brown matrix is composed of (very) poorly sorted, coarse arkosic sand sourced from the granodioritic basement. Bedding is poorly developed and subhorizontal, and may be truncated by palaeochannels. Group 5 is incised by the modern alluvial system and in places forms terraces of unknown (Pleistocene?) age.

Palaeocurrents

The syntectonic basin fill of the Santa Rosa basin contains a number of palaeocurrent indicators (e.g., clast imbrications, foresets) that help constrain the evolution of the basin (Figs 5 and 6). When integrated over the entire basin, the majority of palaeocurrent readings show broadly NW-directed transport with less frequent flow towards SE or NE (Fig. 5 inset). However, significant variations exist that are controlled by geographical location, local topography and stratigraphic level (see individual measurements, shown as black arrows in map of Fig. 5). At the base of the syn-rift strata, palaeotransport occurred in a roughly NW direction at moderate to high angles away from the hanging wall, although minor axial-parallel flow can also be observed (Fig. 5). In SRb3, a change to both NW- and SE-directed transport can be seen near the top of group 3 (Fig. 5). Further SW (SRb1, SRb2), the same NW-SE bidirectional palaeoflow regime does not occur until much later, above the upper basalt and welded tuff (Fig. 5). Although very limited data are available closer to the detachment, a change to SE-directed palaeotransport sourced from the footwall seems probable (Fig. 5). Palaeoflow patterns are somewhat more complicated in the vicinity of the Amarillas transfer zone, which is likely due to the complex structural setting at the intersection of three major faults (Fig. 5).

The palaeocurrent data can be readily interpreted in terms of sediment dispersal in alluvial fans shed from either footwall or hanging wall, or both. This is best shown in a plot of palaeotransport vs. α, the angle between palaeotransport and dip direction of the strata. Due to the general NW tilt of the basin fill, the plot can be used to differentiate between axial-through ($45^{o}<\alpha<135^{o}$ or $225^{o}<\alpha<315^{o}$), hanging wall ($315^{o}<\alpha<45^{o}$) and footwall ($135^{o}<\alpha<225^{o}$) derived drainage (Fig. 6). This classification probably overemphasizes the role of axial-through drainage, because unrestricted alluvial fans tend to spread out from their apex in all possible directions (e.g., Bull, 1972). Nevertheless, Fig. 6 clearly shows that sediment dispersal was dominated by transverse systems. Broadly NW-directed palaeocurrents thus record deposition in coalescing alluvial fans shed from the Sierra Santa Rosa (Fig. 5), while SE-directed palaeocurrents record transport in steeper(?) alluvial fans from the footwall of the Santa Rosa detachment (Fig. 5). The area where palaeoflow was inconsistent (NW- and SE-directed) probably corresponds to the depocentre of the Santa Rosa basin, where the fine-grained distal facies from both footwall and hanging wall was deposited. Minor axial-through drainage along the depocentre cannot be ruled out and is, in fact, quite likely given that the modern fluvial system in the northeastern basin crosscuts the eastern Sierra Santa Rosa in a pre-existing drainage channel (Fig. 5).

Clast statistics

A series of 25 clast point-counts were used to investigate the sediment provenance at different levels within the Santa Rosa basin fill. A summary of clast petrofacies and potential source lithologies is given in Table 2; results of the clast counts are listed in Table 3 and shown in Fig. 7. Outcrop locations and stratigraphic levels are shown in Figs 3 and 5.

Most of the pre-rift deposits accumulated as discontinuous, but more or less evenly distributed lithologies onto the crystalline basement, which is dominated by granodiorite (north) or quartz-diorite (south; Figs 3 and 5). Except for marble and chert, all clasts are exposed (though not exclusively) in the study area (Table 2). Coupled with palaeotransport observations, this indicates that clasts are primarily locally derived, and occasional exotic clasts were probably reworked from the basal sediments. Most lithologies occur in both the foot and hanging wall of the Santa Rosa detachment, and it is difficult to distinguish the two based on clast compositions alone.

Clast assemblages change dramatically between different beds, along-strike the basin and upsection, suggesting a strongly event-controlled sediment supply. In the NE (SRb4), clast statistics record a relatively simple crossover from entirely basaltic (Tmvs; SRb4.5), to mixed basaltic, rhyolitic and granodioritic (Tms_{1-2}; SRb4.3–4.4), to exclusively granodioritic in the fault-scarp facies (SRb4.1; Figs 3 and 7; Table 3). This trend likely reflects a change from fluvial deposition on a low-relief pre-rift surface (SRb4.5) to a tectonically controlled topography dominated by alluvial fans (SRb4.3–4.4). Progressive erosional and tectonic unroofing of both foot and hanging wall exposed successively deeper crustal levels, thereby reducing the influx of volcanic clasts (Fig. 7). The paucity of palaeocurrent data in SRb4 (Fig. 5) and the similarity of lithologies across the detachment make it difficult to establish the relative contributions of foot and hanging wall catchments.

In the central Santa Rosa basin, clasts of a pre-rift volcaniclastic conglomerate (Tmvc) below the andesite are exclusively derived from the underlying Tuff of San Felipe (SRb3.5; Fig. 7; Table 3). Unlike in SRb4, the megabreccia at the base of group 3 is composed entirely of granodiorite clasts (SRb3.4), and assemblages shift to volcanic-dominated higher in the section (SRb3.1; Fig. 7; Table 3). This probably indicates a change from colluvial deposition at the base of the nascent Santa Rosa escarpment to foot and hanging wall-derived alluvial fans, which are represented by mixed volcanic and granodioritic assemblages that include up to 5% of quartz-diorite from the footwall (Figs 5 and 7). The top-most clast-count is

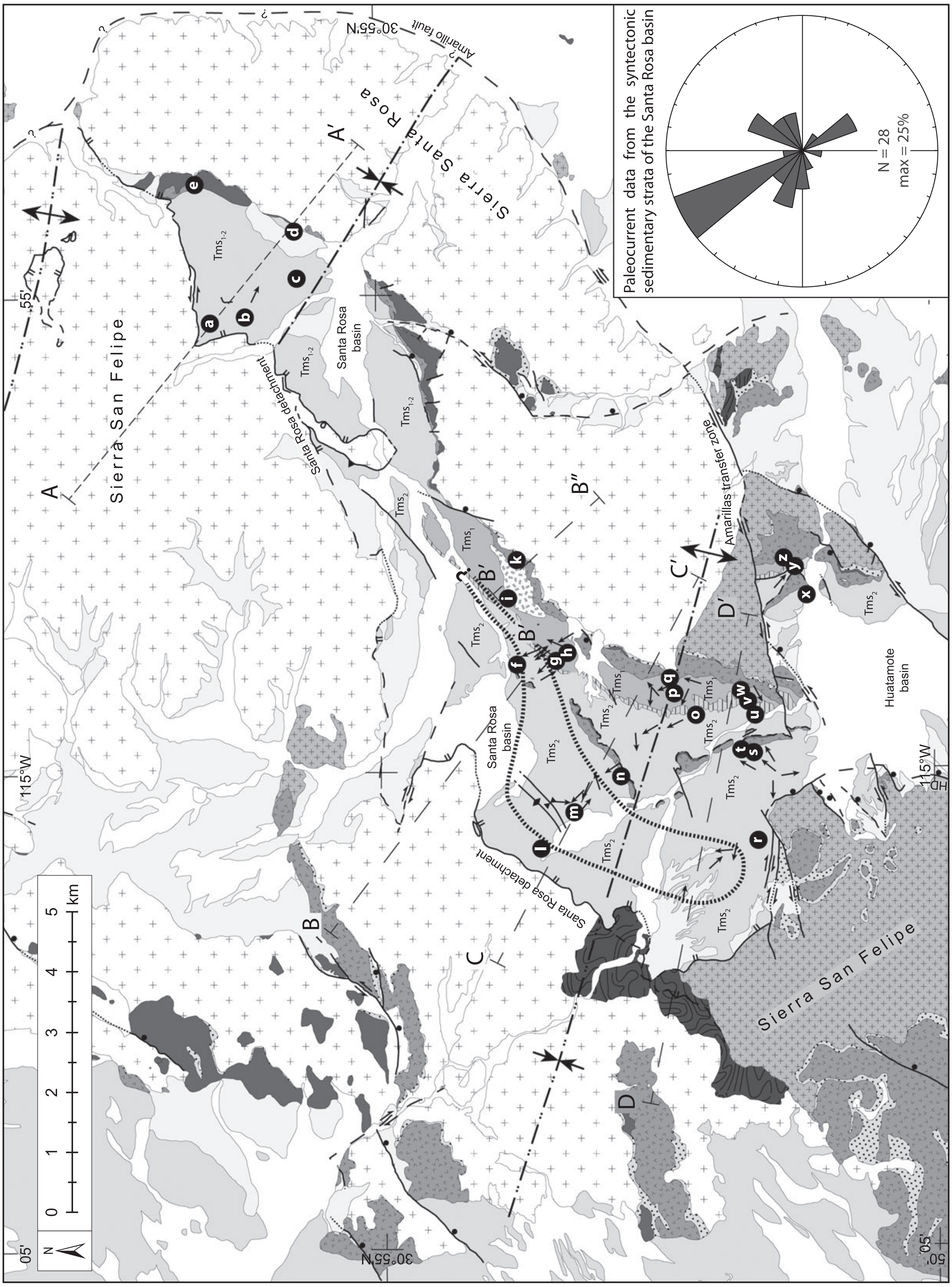

Fig. 5. Geological map of the study area showing the locations of clast point-count statistics (filled circles with letters) and cross sections (Fig. 10). Palaeoflow measurements are drawn as black arrows and summarized in a rose diagram (inset). The approximate extent of the depocentre facies is shown as a thick hashed outline. See Fig. 2 for legend.

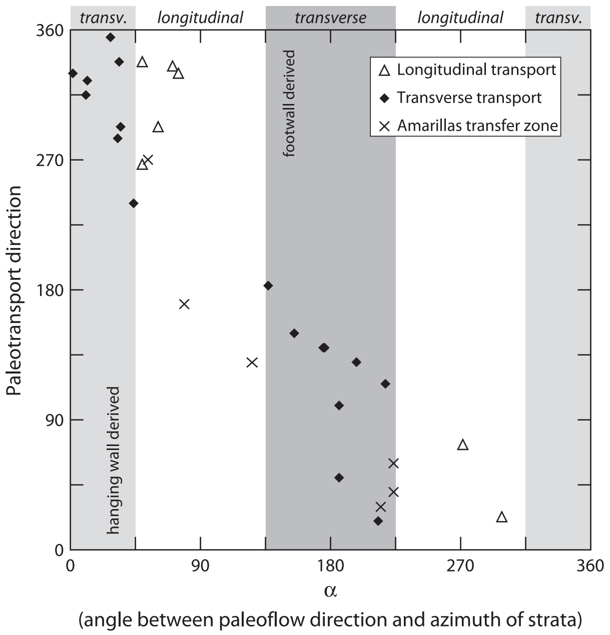

Fig. 6. Plot of palaeocurrent direction vs. α, the angle between palaeotransport and dip direction of the strata. The plot makes use of the overall NW-tilt of the basin-fill to differentiate between axial (45°<α<135° or 225°<α<315°), hanging wall (315°<α<45°) and footwall-derived (135°<α<225°) drainage. The diagram shows that sediment dispersal occurred predominantly in a transverse direction (i.e. perpendicular to the margin of the basin).

dominated by gravel from the Tuff of San Felipe (*ca*. 90%; SRb3.1; Fig. 7; Table 3), which is somewhat unexpected given that (a) the associated conglomerate occurs below the upper basalt and tuff (Figs 3d and 7), and (b) all potential source lithologies were well exposed at that stage.

Elsewhere in the Santa Rosa basin, clast assemblages more closely resemble the patterns of SRb4. In SRb2, clast compositions are dominantly volcanic near the base (SRb2.4–2.6) but change to granodiorite > welded tuff upsection (SRb2.1–2.2; Fig. 7; Table 3). A similar trend from volcanic-rich (SRb1.5–1.6) to volcanic-poor (SRb1.1, 1.3) can also be seen further SW, although large variations exist along-strike and between beds (e.g. SRb1.2, SRb1.3) that are likely associated with the detachment–transfer fault intersection there (Figs 5 and 7; Table 3). Throughout the SW basin (SRb1, Hb1), conglomerates contain a sizeable percentage of quartz-diorite and occasionally metamorphic clasts from the local substrate (Figs 5 and 7; Table 3). The fact that such clasts are rare elsewhere in the basin is consistent with the proposed transverse-dominated drainage regime. Some beds (e.g. SRb1.6) also contain a significant portion of metamorphic clasts that are not exposed in the immediate catchment area (Fig. 5). These clasts are most likely reworked from the basal sediment, which contains >35% metamorphic gravel (Bryant, 1986) and makes up *ca*. 10% of all clasts here. Further upsection, an increased influx of batholithic clasts suggests progressively deeper hanging wall incision (SRb1.4–1.5) and a change to footwall-derived drainage (SRb1.1–1.3, SRb2.1–2.3; Fig. 7). The relatively large percentage of volcanic and reworked sedimentary clasts in SRb1.1–1.2, elsewhere attributed to a hanging wall source, are probably sourced from group 1 and 2 strata in the nearby Huatamote footwall (Figs 5 and 7).

Basin architecture

The syntectonic strata of the Santa Rosa basin record some important spatial and temporal variations in the basin architecture. Overall, the basin shows a pronounced along-strike change in grain size, from conglomerate in the NE to sandstone-mudstone in the SW (Fig. 3). The thickest section of group 3 deposits is located in the central basin (SRb2, SRb3) and records the most rapid subsidence at that time (Fig. 3c and d). Group 3 gradually thins further to the SW, which corresponds to a progressively later onset of coarse clastic deposition there (SRb1, Hb1; Fig. 3a and b). Above the air fall tuff (Tmt), maximum subsidence shifts SW-ward through time, first localizing in SRb2 (below group 4 volcanics) before migrating to SRb1 (above group 4 volcanics; Fig. 3b–d). The fine-grained depocentre facies first develops in the central Santa Rosa basin (SRb3) and also shows a systematic SW-ward migration through time. Above the depocentre facies, the conglomerate appears to encroach from the NE, although that probably reflects southeastward progradation of alluvial fans from the detachment footwall (Fig. 3).

The thick section of conglomerate in the NE (SRb4) does not display the retrogradational fining-up pattern seen elsewhere, which may be explained by higher sediment influx, steeper alluvial fans, and/or increased uplift and denudation (Fig. 3e). In any case, the lack of fine-grained facies suggests that the NE was topographically higher than the SW throughout the history of the basin. This is also supported by the fact that marker horizons such as the ash fall tuff (Tmt), which can be correlated throughout the central and SW portions of the basin, are not observed on this high-standing margin.

^{40}AR/^{39}AR GEOCHRONOLOGY

The $^{40}Ar/^{39}Ar$ method was used to date nine samples from all volcanic units of the study area, thus providing a temporal framework for the evolution of the Santa Rosa basin (Fig. 2; Table 4). Two whole-rock samples (sample numbers in brackets) were collected from the base and top of the group 2 olivine basalt (11, 14) in the NE basin to determine the age range of basaltic volcanism (Fig. 2; Table 4). Three samples were collected in the central Santa Rosa basin to date the upper group 2 Tuff of San Felipe (42) and the overlying andesite flow (37, 41; Fig. 2; Table 4). A further three samples (24, 26, 29) constrain the ages of the volcanic units intercalated within the syntectonic basin-fill (Fig. 2; Table 4). A final sample (34)

Table 2. Clast petrofacies and provenance in the Santa Rosa basin

Classification	Abbrev.	Petrofacies	Comments	Source	Hanging wall	Foot-wall	Distal
granodiorite	lc-gd	leuco-granodiorite	leucocratic, rare macroscopic biotite/hornblende	granodiorite, tonalite, pegmatite, aplite (Kgd)*	x	x	x
	bt-gd	biotite-granodiorite	biotite and hornblende bearing	granodiorite, tonalite, pegmatite, aplite (Kgd)*	x	x	x
quartz-diorite	qd	quartz-diorite	mesocratic, biotite and hornblende bearing	quartz-diorite (Kqd)*	x	x	x
metamorphic rocks	qz	quartzite		pre-batholithic metamorphic rocks (pbs)*		x	x
	sch	schist	(psammo-)pelitic quartz-mica schist	pre-batholithic metamorphic rocks (pbs)*		x	x
	lmst	limestone (metamorphic)		pre-batholithic metamorphic rocks (pbs)*			x
	cht	chert		pre-batholithic metamorphic rocks (pbs)*			x
basic volcanic	bs	basalt	aphanitic, ± phenocrysts of olivine	olivine basalt (Tmb_1, Tmb_2)	x	x	
	vbs	basalt (vesicular)	vesicular	olivine basalt (Tmb_1, Tmb_2)	x	x	
	and	andesite	aphanitic, ± phenocrysts of hornblende	hornblende andesite (Tma)	x		
silicic volcanic	rh	rhyolite tuff (welded)		welded rhyolite tuffs (Tmsf, Tmr)	x	x	x
	rht	rhyolite tuff (non-welded)		rhyolitic ash fall tuff (Tmt)	x		
reworked sedimentary	volag	voclanic agglomerate		exotic, basal sediments (Tos)	x	?	?
	sst	sandstone		basal sediments/basin-fill (Tos, Tms_1, Tms_2)	x	x	x
	car	carbonate	unmetamorphosed limestone	basal sediments (Tos)	x	?	

*possibly reworked from basal sediments (Tos).

was collected from a deformed basalt intrusion (Tmb_i) at the base of a tectonic klippe bounded by the Santa Rosa detachment in the NE (Fig. 2; Table 4). Analytical details of the $^{40}Ar/^{39}Ar$ analyses are described in the appendix; sample details and results from step-heating experiments are given in Tables 4 and 5, and age spectra are plotted in Fig. 8. Details from individual experiments and representative blank measurements are available as Supplementary Tables S1 and S2. For ease of comparison with published K-Ar and $^{40}Ar/^{39}Ar$ ages, final $^{40}Ar/^{39}Ar$ ages are reported with 2σ errors in the text and in Table 6, which includes the uncertainty in the J-value. All other values, including plateau ages shown in Fig. 8 and reported in Tables 4 and S1, are given with 1σ uncertainties unless stated otherwise.

$^{40}Ar/^{39}Ar$ results

Ages of volcanic rocks in the study area range from Early to Late Miocene (*ca*. 21–7 Ma) and are, with the exception of the upper basalt (Tmb_2) and welded tuff (Tmr), consistent with stratigraphic levels. All samples exhibit relatively simple and readily interpretable release spectra that yield well-defined plateau ages interpreted as eruption ages of the volcanics.

Group 2 volcanic rocks

Whole-rock analyses of samples 11 (base) and 14 (top) of the lower olivine basalt (Tmb_1) yielded plateau ages of 19.30 ± 0.22 Ma and 18.67 ± 0.18 Ma, respectively (Fig. 8a and b; Table 5). The plateau ages differ at the 2σ level, which suggests a gap of *ca*. 0.5–1 Ma between the two basalt flows; this is reasonable given that the two flows are separated by a <5–10 m thick sandstone unit at this location. Step-heating analysis of sanidine from the Tuff of San Felipe (sample 42) produced a well-defined plateau age of 12.87 ± 0.20 Ma encompassing 96.2% of the total ^{39}Ar released (Fig. 8h; Table 5).

Two samples were collected from the base (41) and top (37) of the hornblende andesite flow (Tma) in the central Santa Rosa basin (Fig. 2). Incremental step-heating experiments yielded indistinguishable plateau ages of 9.51 ± 0.70 Ma (91.0% of ^{39}Ar) and 9.35 ± 0.14 Ma (60.6% of ^{39}Ar) for hornblende (41, base) and plagioclase (37, top), respectively, with an integrated weighted mean

Table 3. Clast-count statistics for conglomerate and breccia in the Santa Rosa basin

			Frequency of clasts counted [%]															
			grano-/quartzdiorite			*metamorphic rocks*				*basic volcanic*			*silicic vol.*		*reworked sedim.*			
ID	Section	Unit	lc-gd	bt-gd	qd	qz	sch	lmst	cht	bs	vbs	and	rh	rht	volag	sst	car	N
a	SRb4.1	Tms_{1-2}	–	100.0	–	–	–	–	–	–	–	–	–	–	–	–	–	200
b	SRb4.2	Tms_{1-2}	6.1	89.2	1.4	–	–	–	–	1.4	–	–	1.9	–	–	–	–	212
c	SRb4.3	Tms_{1-2}	7.1	62.8	7.4	–	–	–	–	12.1	–	–	10.6	–	–	–	–	282
d	SRb4.4	Tms_{1-2}	1.2	5.0	–	1.2	–	–	–	70.0	6.9	–	15.7	–	–	–	–	260
e	SRb4.5	Tmvc	–	–	–	–	–	–	–	54.5	45.5	–	–	–	–	–	–	200
f	SRb3.1	Tms_2	–	1.3	–	–	–	–	–	9.1	–	–	89.6	–	–	–	–	77
g	SRb3.2	Tms_1	7.1	26.7	5.1	1.6	–	1.6	–	14.6	1.2	–	39.3	–	2.0	0.8	–	254
h	SRb3.3	Tms_1	48.0	29.4	–	–	–	–	–	0.4	–	0.4	21.8	–	–	–	–	271
i	SRb3.4	Tms_1	–	98.0	–	–	–	–	–	–	–	1.0	1.0	–	–	–	–	est
k	SRb3.5	Tmvc	–	–	–	–	–	–	–	–	–	–	100.0	–	–	–	–	est
l	SRb2.1	Tms_2	18.4	49.8	–	–	–	–	–	0.4	–	–	31.4	–	–	–	–	223
m	SRb2.2	Tms_2	5.7	74.8	–	–	–	–	–	0.4	–	–	18.7	–	–	0.4	–	262
n	SRb2.3	Tms_2	2.9	56.7	0.4	2.1	–	–	–	10.7	0.8	–	22.3	–	0.8	3.3	–	242
o	SRb2.4	Tms_2	2.1	3.7	0.8	2.9	–	0.8	–	5.8	–	–	83.9	–	–	–	–	242
p	SRb2.5	Tms_1	3.9	15.4	9.8	0.8	–	1.6	–	13.8	–	–	48.4	–	2.0	4.3	–	254
q	SRb2.6	Tms_1	6.6	2.8	–	4.7	–	2.4	0.5	19.3	1.9	–	60.9	–	0.9	–	–	212
r	SRb1.1	Tms_2	13.7	21.6	4.7	3.0	4.3	–	6.4	16.7	0.9	–	15.0	–	11.6	2.1	–	233
s	SRb1.2	Tms_2	3.0	10.6	3.4	–	1.9	–	–	20.8	4.5	–	55.8	–	–	–	–	264
t	SRb1.3	Tms_2	11.1	23.2	1.4	2.1	39.4	3.5	1.0	2.8	1.4	–	1.7	–	1.7	10.4	0.3	289
u	SRb1.4	Tms_2	2.1	38.9	16.9	–	1.7	–	4.2	13.1	–	–	16.0	0.4	6.3	0.4	–	237
v	SRb1.5	Tms_1	4.7	20.7	16.5	–	2.4	0.4	2.0	2.4	0.8	–	47.7	–	1.6	0.8	–	255
w	SRb1.6	Tms_1	3.3	5.9	2.0	–	6.5	2.6	1.6	7.2	0.7	–	59.4	–	5.6	4.9	0.3	306
x	Hb1.1	Tms_2	3.2	2.9	0.7	–	0.7	0.4	–	15.2	3.2	–	73.3	–	–	0.4	–	277
y	Hb1.2	Tms_2	1.3	–	30.2	–	–	–	–	4.0	–	–	64.5	–	–	–	–	225
z	Hb1.3	Tms_1	0.5	–	1.0	–	–	–	–	1.9	–	–	96.6	–	–	–	–	209

Abbreviations of petrofacies are explained in Table 2. Point-counts were conducted by determining the lithology of any clast > 5 mm in diameter at 10 cm intervals over a distance of 30 m. est=estimated.

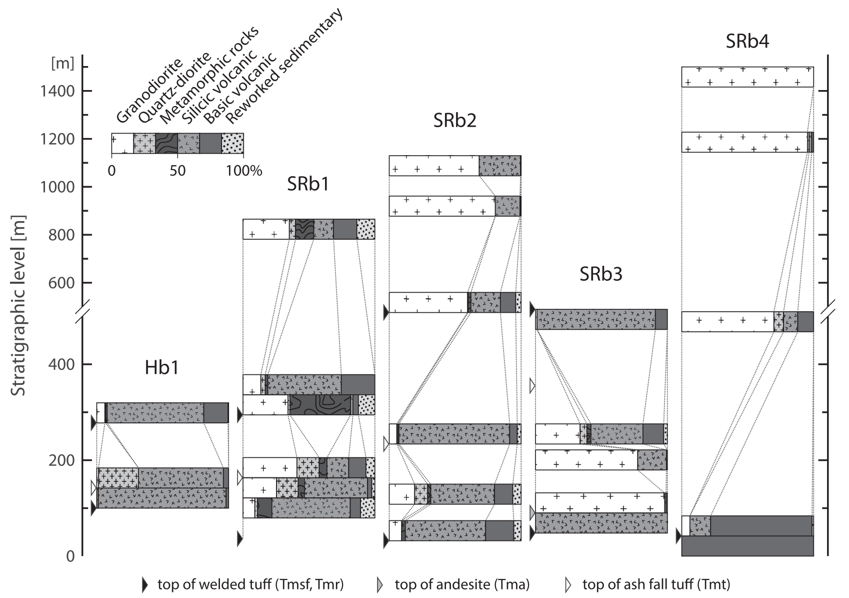

Fig. 7. Representative clast composition measurements of conglomerate beds in the Santa Rosa basin arranged according to their stratigraphic location. See Figs. 3 and 5 for point-count locations and Table 3 for data. The top of intercalated volcanic units is shown by arrowheads. SRb1 = Santa Rosa basin section 1, SRb2 = Santa Rosa basin section 2, SRb3 = Santa Rosa basin section 3, SRb4 = Santa Rosa basin section 4, Hb1 = Huatamote basin section 1.

Table 4. $^{40}Ar/^{39}Ar$ sample details

Sample	Longitude	Latitude	Rock type	Unit	Mineral	Comments
11	−114.92236	30.91344	ol-basalt	Tmb_1	wr	base of Tmb_1, *ca.* 20m above basement
14	−114.92211	30.91441	ol-basalt	Tmb_1	wr	top of Tmb_1, *ca.* 8m below Tmsf
24	−115.00084	30.88071	welded rhyolite tuff	Tmr	sd ($or_{54}ab_{46}$)	welded rhyolite tuff, no eutaxitic foliation
26	−115.00084	30.88071	ol-basalt	Tmb_2	wr	
29	−114.96418	30.85549	rhyolite tuff	Tmt	sd ($or_{51}ab_{49}$)	base of Tmt, contains *ca.* 20% lithics
34	−114.91400	30.96974	basalt	Tmb_i	bt	intrusion in footwall, deformed by detachment
37	−114.96928	30.89749	hbl-andesite	Tma	pl	top of Tma, *ca.* 5m below Tms_1
41	−114.96364	30.89572	hbl-andesite	Tma	hbl	base of Tma, *ca.* 5m above Tmsf
42	−114.96343	30.89559	welded rhyolite tuff	Tmsf	sd ($or_{53}ab_{47}$)	top of Tmsf (Tuff of San Felipe), *ca.* 8m below Tma

ab=albite, bt=biotite, hbl=hornblende, ol=olivine, or=orthoclase, pl=plagioclase, sd=sanidine, wr=whole rock.

Table 5. Summary[a] of $^{40}Ar/^{39}Ar$ furnace step heating results

			Plateau age					Inverse isochron age			
Sample	Unit	Steps	Interval [ºC]	Cum % ^{39}Ar	MSWD	p	Age ± 1σ [Ma]	$^{40}Ar/^{36}Ar_i \pm 1\sigma$	MSWD	p	Age ± 1σ [Ma]
11	Tmb_1	11–15	1100–1300	53.8	0.78	0.54	19.30 ± 0.11	316 ± 63	0.93	0.42	19.05 ± 0.43
14	Tmb_1	12–17	1050–1350	72.9	1.80	0.11	18.67 ± 0.09	321 ± 35	1.70	0.15	18.18 ± 0.35
24	Tmr	6–16	850–1350	93.8	0.57	0.84	12.56 ± 0.07	359 ± 110	0.43	0.92	12.21 ± 0.36
26	Tmb_2	4–9	750–1200	74.6	0.77	0.57	20.98 ± 0.11	330 ± 95	0.81	0.52	20.90 ± 0.18
29	Tmt	6–16	850–1350	98.1	0.53	0.87	6.78 ± 0.06	294 ± 6	0.54	0.84	6.79 ± 0.06
34	Tmb_i	4–13	750–1450	98.5	1.30	0.24	17.04 ± 0.08	282 ± 38	1.40	0.19	17.09 ± 0.13
37	Tma	3–10	750–1300	60.6	1.50	0.18	9.35 ± 0.07	300 ± 5	1.30	0.27	9.22 ± 0.11
41	Tma	4–13	1030–1450	91.0	0.24	0.99	9.51 ± 0.35	291 ± 11	0.64	0.74	10.00 ± 0.80
42	Tmsf	4–16	750–1350	96.2	0.51	0.91	12.87 ± 0.10	299 ± 6	0.48	0.92	12.80 ± 0.12

[a]Full analytical dataset available as Supplementary Tables S1 and S2.

age of 9.36 ± 0.14 Ma (Fig. 8g; Table 5). The plagioclase release spectrum (37) shows a slight saddle-shaped pattern with older ages at the low- and high-temperature portions of the gas release, suggesting that a minor amount of excess argon may have been present in the system (Fig. 8g). However, the plagioclase plateau age at the base of the saddle (9.35 ± 0.14 Ma) is consistent with the flat hornblende age spectrum (9.51 ± 0.70 Ma), suggesting that excess argon had little effect on the plateau age itself.

Group 3 and 4 volcanic rocks

Sanidine was extracted from the ash fall tuff (Tmt) that caps the syntectonic group 3 deposits in the Santa Rosa basin (29; Fig. 2). Step-heating analysis yielded a plateau age of 6.78 ± 0.12 Ma, which incorporates 98.1% of the total ^{39}Ar released (Fig. 8e; Table 5).

Step heating of fresh whole-rock chips collected from an intact, boulder-sized fragment of the upper olivine basalt (Tmb_2), produced a concordant spectrum with a plateau age of 20.98 ± 0.22 Ma (74.6% of total ^{39}Ar) between 750 –1200°C (26; Fig. 8d; Table 5). The low- and high-temperature part of the spectrum contains some anomalous steps with much younger ages; however, individual steps are all significantly older than the 6.78 ± 0.12 Ma plateau age of the underlying ash fall tuff (Fig. 8d; Table 5).

Sanidine was separated from a nonbrecciated, nonfoliated spherulitic section of the upper welded tuff (Tmr) to avoid potential contamination by lithics from the visually analogous Tuff of San Felipe. The release spectrum of sample 24 produced a very well-defined plateau age of 12.56 ± 0.14 Ma that incorporates 93.3% of the total ^{39}Ar released (Fig. 8c; Table 5).

Deformed olivine basalt

Sample 34 was collected from a basalt dike (Tmb) that was deformed by the Santa Rosa detachment in the NE of the study area (Fig. 2). Step heating of biotite produced a concordant spectrum with a plateau age of 17.04 ± 0.16 Ma, incorporating 98.5% of the total ^{39}Ar released (Fig. 8f; Table 5).

Comparison to previous geochronology

The $^{40}Ar/^{39}Ar$ results reported here provide an important temporal framework for the interpretation of the Santa Rosa basin and resolve some long-standing uncertainties associated with conflicting ages in the basin (Table 6). The Early Miocene (19.30 ± 0.22 Ma, 18.67 ± 0.18 Ma) ages of the lower basalt (Tmb_1) are significantly older than the 15.0 ± 0.4 Ma age previously reported for the same unit in the SW basin (Table 6; Gastil *et al.*, 1979). Basal-

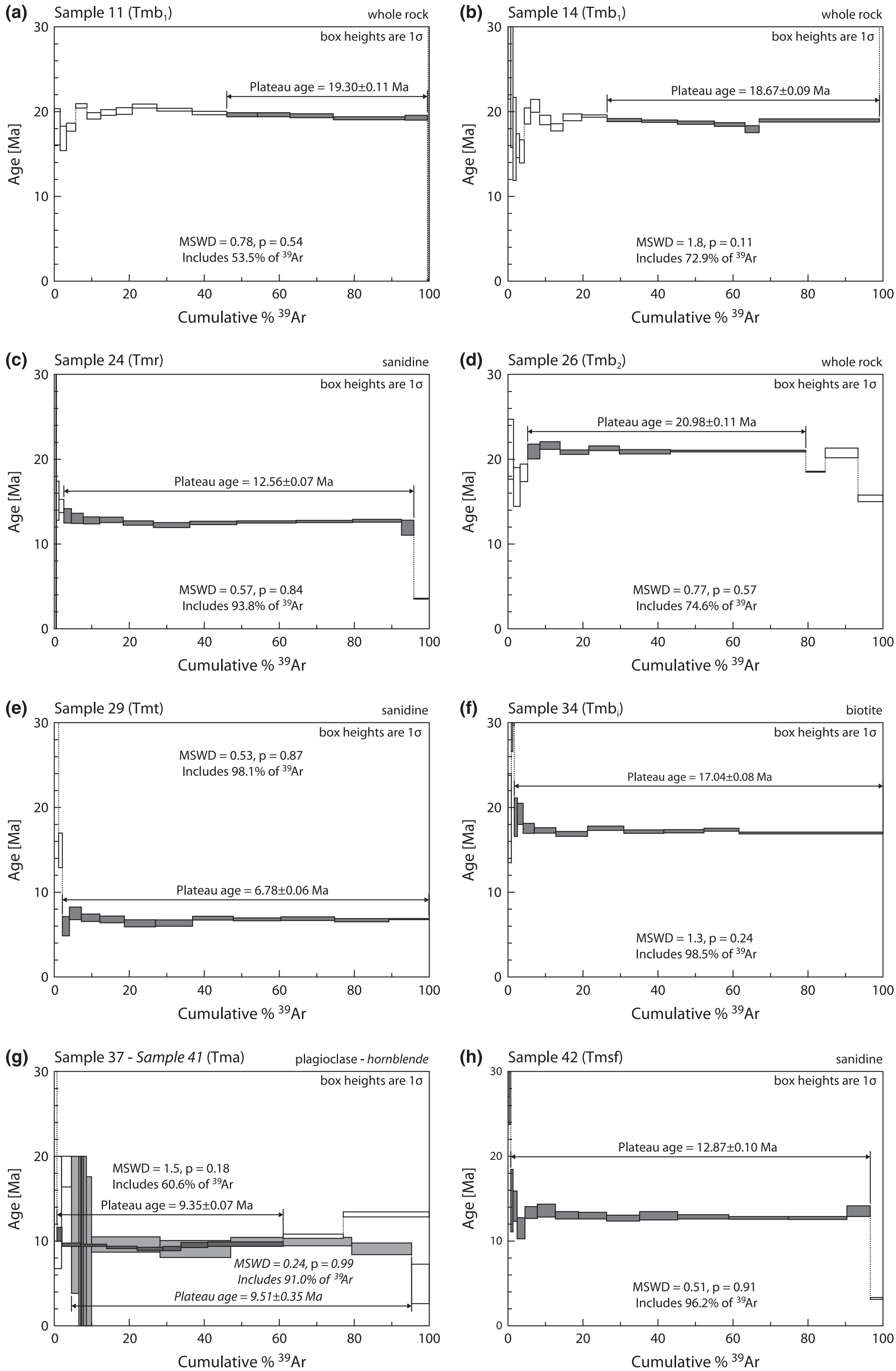

Fig. 8. $^{40}Ar/^{39}Ar$ release spectra and plateau ages (1σ error) of volcanic rocks from the Santa Rosa basin. Sample locations are shown in Fig. 2, unit abbreviations are the same as in Table 4.

Table 6. Comparison of available geochronological data for volcanic rocks of the Santa Rosa basin

		Gastil *et al.* (1979)		Bryant (1986)		Stock *et al.* (1999)		This study	
Unit	Rock type	Mineral	Age ± 2σ [Ma]	Mineral	Age ± 2σ [Ma]	Mineral	Age ± 2σ [Ma]	Mineral	Age ± 2σ [Ma]
Tmb_1	ol-basalt	wr[a]	15.0 ± 0.4					wr[b]	19.30 ± 0.22
Tmsf[c]	welded rhyolite tuff	wr[a]	14.2 ± 0.9	sd[a]	2.3 ± 0.2	sd[b]	12.43 ± 0.28	sd[b]	12.87 ± 0.20
Tma	hbl-andesite			pl[a]	9.0 ± 0.7			pl/hbl[b]	9.36 ± 0.14
Tmt	rhyolite tuff			wr[a]	16.6 ± 1.3			sd[b]	6.78 ± 0.12
Tmb_2	ol-basalt	pl[a]	8.9 ± 1.2					wr[b]	20.98 ± 0.22
Tmr[c]	welded rhyolite tuff			wr[a]	12.3 ± 1.8			sd[b]	12.56 ± 0.14

hbl=hornblende, ol=olivine, pl=plagioclase, sd=sanidine, wr=whole rock.
[a]Dated using K-Ar technique.
[b]Dated using $^{40}Ar/^{39}Ar$ technique.
[c]Units correlated in this study (Tuff of San Felipe).

tic volcanics in comparable stratigraphic positions elsewhere in NE Baja California yield ages ranging between *ca*. 21 and 15 Ma (e.g., Stock, 1989; Lee *et al.*, 1996; Lewis, 1996; Nagy *et al.*, 1999; Esser & McIntosh, 2003) and are part of a Miocene belt of calc-alkaline volcanic rocks along the E margin of Baja California (equivalent to the Comondú volcanic arc in southern Baja California; e.g., Hausback, 1984; Sawlan, 1991). It is possible that the basalt of Gastil *et al.* (1979) represents a different (younger) flow of Tmb_1 than those dated here.

The Tuff of San Felipe in the central Santa Rosa basin yielded a plateau age of 12.87 ± 0.20 Ma, which is slightly older than the weighted mean age of 12.43 ± 0.14 Ma (K-feldspar total fusion) reported by Stock *et al.* (1999) for the SW basin, but younger than a K-Ar whole rock age (14.2 ± 0.9 Ma) from the basal vitrophyre (Table 6; Gastil *et al.*, 1979). Elsewhere, dating of the Tuff of San Felipe resulted in a somewhat disparate spread of eruption ages ranging from 16.7 ± 1.0 Ma to 9.1 ± 0.5 Ma (see Stock *et al.*, 1999). Although these discrepancies are difficult to reconcile, Stock *et al.* (1999) argued for an age of *ca*. 12.6 Ma for the Tuff of San Felipe, which is consistent with most of the data available and does not conflict with any of the over- or underlying units. Our results essentially corroborate their interpretation, although a slightly older age seems possible according to our data.

The andesite flow (Tma) of the central Santa Rosa basin previously yielded a plagioclase K-Ar age of 9.0 ± 0.7 Ma (Bryant, 1986), which is within error of our weighted mean age of 9.36 ± 0.14 Ma (Table 6).

The 6.78 ± 0.12 Ma plateau age calculated for the rhyolitic ash fall tuff (Tmt) that caps group 3 differs markedly from the 16.6 ± 0.3 Ma age (K-Ar whole rock) of Bryant (1986) for this unit (Table 6). The latter is significantly older than the underlying andesite (9.36 ± 0.14 Ma) and Tuff of San Felipe (*ca*. 12.6 Ma) and is deemed erroneous (Table 6). By comparison, our age is consistent with the stratigraphic level of Tmt and coincides with a period of known rhyolitic volcanism in the Puertecitos Volcanic Province to the south (e.g., Martín-Barajas *et al.*, 1995; Lewis, 1996; Nagy *et al.*, 1999).

Prior to our study, K-Ar dating of plagioclase from the upper basalt (Tmb_2) gave an age of 8.9 ± 1.2 Ma (Gastil *et al.*, 1979), while K-Ar whole rock analyses of the overlying ignimbrite yielded ages of 13.6 ± 2.4 Ma and 12.3 ± 1.8 Ma, respectively, for the basal vitrophyre and the rhyolite (Table 6; Bryant, 1986). Our $^{40}Ar/^{39}Ar$ whole rock experiments indicate a substantially older age of 20.98 ± 0.22 Ma for the upper basalt, whereas sanidine from the welded rhyolite yielded a more precise age of 12.56 ± 0.14 Ma, essentially identical to the aforementioned K-Ar results for that unit (Table 6). All of these ages conflict with the apparent stratigraphic level of the two volcanics (see discussion below).

DUPLICATION OF THE PRE-RIFT VOLCANIC STRATA – A HANGING WALL-DERIVED GRAVITY SLIDE BLOCK

One of the key problems with earlier geochronology data from the Santa Rosa basin was that several of the K-Ar ages were in apparent conflict with the stratigraphic level of the dated units. While our work has shown that some of those results were indeed problematic (e.g., Tmt, Tmb_2), other ages (e.g., Tmr) are consistent with the results of this study. In fact, our data show that both the upper basalt (Tmb_2; 20.98 Ma) and welded tuff (Tmr; 12.56 Ma) are older than the stratigraphically lower ash fall tuff (Tmt; 6.78 Ma) and andesite (Tma; 9.36 Ma). Instead, group 4 volcanics appear to duplicate the ages of the pre-rift group 2 basalt and the Tuff of San Felipe: Both basalts are Early Miocene (*ca*. 19 Ma vs. 20.98 Ma), while the two ignimbrites are Middle Miocene (12.87 Ma vs. 12.56 Ma, indistinct at 2σ). Given the locally fragmented appearance of the group 4 basalt and rhyolite, it is in theory possible that we and Bryant (1986) have inadvertently sampled lithic fragments derived from the group 2 basalt and rhyolite. However, we reject this scenario because (a) special care was taken in the field to avoid sampling lithic fragments, and (b) all five group 4 samples predate the underlying 6.78 Ma old ash fall tuff of group 3, and most also predate the 9.36 Ma andesite of group 2.

Given the similarity in appearance of nonbrecciated sections (i.e., colour, crystal content, abundance of lithics and degree of welding) and the (nearly) identical ages, we propose that the group 4 basalt and ignimbrite represent a stratigraphic repetition of the group 2 basalt and Tuff of San Felipe. We interpret the group 4 volcanics as allochthonous, gravity-driven slide block deposits (here named the Santa Rosa slide) that originated from an elevated head in the NW-tilted hanging wall (Sierra Santa Rosa) during the latest Miocene or Pliocene, sometime after 6.78 Ma. A small-scale equivalent of such slide blocks is exposed in the NE basin (N30.9143º, W114.9196º), where, over a strike-length of *ca*. 200 m, the strongly tilted Early Miocene basalt (Tmb_1) and the Tuff of San Felipe (Tmsf) are overlain by two separate basalt-ignimbrite couplets that are indubitably stratigraphic repetitions (Fig. 4h).

Large gravity-driven slide blocks are common in tectonically active areas such as the Basin and Range in places where a high vertical relief coincides with structural or stratigraphic anisotropies that may act as pre-existing weakness zones (e.g. Boyer & Hossack, 1992; Topping, 1993; Davis & Friedmann, 2005). In case of the Santa Rosa slide, slide detachment may have been assisted by an earthquake, given the previously described observations for palaeoseismicity and the relatively lowslope angle (<16º) at the time of emplacement. During emplacement, the Santa Rosa slide probably became segmented into several internally coherent slabs that moved between *ca*. 1–3 km down-slope and resulted in the discontinuous exposure of today. Although the internal stratigraphy is intact and concordant with the sediments below and above, both the basalt and ignimbrite are pervasively fragmented. Differential motion between clasts varies but is often minor, resulting in a fitted 'jigsaw' fabric. Typical features of slide sheets such as knife-sharp basal contacts with planar fault-like surfaces, striations and slickensides, soft-sediment deformation, intermixing of substrate with slide deposits, clastic dikes and partially pulverized breccia at the base of the slide block (e.g., Yarnold & Lombard, 1989; Topping, 1993; Friedmann, 1997; Anders *et al.*, 2000; Davis & Friedmann, 2005) are either lacking or difficult to distinguish from primary volcanic emplacement features.

ONSET OF DEFORMATION AND SEDIMENTATION RATES

Stratigraphic relationships and geochronology data presented here provide some key constraints on the timing of basin initiation and thus deformation on the Santa Rosa detachment, which until recently was very poorly constrained. Seiler *et al.* (2011) used apatite fission track and (U-Th)/He thermochronology to constrain the exhumation history of the Santa Rosa detachment and date fault slip. Six samples from the footwall yielded fission track ages between 46 ± 2 Ma and 16 ± 1 Ma (1σ) and two (U-Th)/He ages of 41 ± 4 Ma and 6 ± 1 Ma (2σ). Most of their ages are older than the onset of rifting and cannot be used as direct age constraints. However, by utilizing the time-temperature relationship that controls fission track annealing, Seiler *et al.* (2011) were able to model the thermal evolution of the samples and thus the footwall uplift history. Their models show that detachment slip began after *ca*. 10–8 Ma and before *ca*. 7–0 Ma, with the best constrained models suggesting an onset age of *ca*. 9–7 Ma, which is consistent with an apatite (U-Th)/He cooling age of 6 ± 1 Ma.

Our $^{40}Ar/^{39}Ar$ analyses allow us to revisit some of the discrepancies of previous K-Ar ages and independently constrain the onset of faulting on the Santa Rosa detachment. The earliest stratigraphic record of detachment activity is the monolithologic megabreccia at the base of group 3 in the central Santa Rosa basin (Bryant, 1986; this study). The megabreccia directly overlies and thus postdates the 9.36 ± 0.14 Ma andesite flow and predates the 6.78 ± 0.12 Ma group 3 ash fall tuff, which lies *ca*. 160 m stratigraphically above the top of the megabreccia. This suggests that slip on the central detachment initiated relatively soon after 9.36 Ma, and certainly well before eruption of the tuff to allow for the accumulation of *ca*. 200 m of syntectonic sediment by 6.78 Ma. Initiation of slip between 9.36 Ma and 6.78 Ma provides strong support for the interpretation of Seiler *et al.* (2011), who had argued that detachment faulting began between *ca*. 9–7 Ma. Subhorizontal Quaternary terraces of group 5 drape the projected trace of the Santa Rosa detachment in several places, suggesting that fault slip ceased during the Late Plio- to Pleistocene.

By assuming detachment onset and cessation ages of 9.36 and 1.8 Ma, respectively, we can compare minimum sedimentation rates for the syn-rift strata of groups 3 and 4 in different parts of the basin. Integrated group 3 sedimentation rates appear to decrease southwestward from a maximum of *ca*. 100 m/Ma in SRb3 to *ca*. 10 m/Ma south of the Amarillas transfer zone (Hb1) if subsidence occurred synchronously in all sections. Alternatively, rates in the SW may have been higher (similar to SRb3?), but subsidence (and by extension faulting) began progressively later towards the SW basin as the detachment grew along strike. This interpretation is supported by the different lithofacies found at the base of group 3 in the central Santa Rosa basin (breccia and conglomerate) compared with the southwestern basin (sand and mud; Fig. 3). Rates for the upper syn-rift sequence (group 4) are roughly comparable in sections Hb1 and SRb3 (*ca*. 80–100 m/Ma), similar to the maximum rates during group 3 deposition, but are significantly larger (200–350 m/Ma) in the SW portion of the basin (SRb1-2).

We interpret these patterns to indicate that the central Santa Rosa basin (SRb3) experienced relatively steady sedimentation at more or less constant rates beginning shortly after deposition of the *ca*. 9.36 Ma andesite flow. Alternatively, early (group 3) sedimentation rates were significantly higher than the *ca*. 100 m/Ma calculated above, which would imply that faulting started slightly later than *ca*. 9 Ma, perhaps as late as *ca*. 8–7.5 Ma using maximum rates (*ca*. 200–350 m/Ma) experienced during the later stages of basin formation. In either case, this central region was the main locus of subsidence and sedimentation during the early phase of rifting. After *ca*. 6.78 Ma, maximum subsidence shifted towards the SW basin (SRb1-2) to define a depocentre in the hanging wall above the synformal hinge region of the Santa Rosa detachment near the SW basin margin, with sedimentation rates that increased up to six-fold there.

TIMING OF TILTING

An intriguing aspect of the Santa Rosa basin is the fact that in some areas, group 3 strata at the base of the section are only marginally – if at all – more steeply tilted than the uppermost group 4 strata (Figs 2 and 9a). In SRb1, bedding dips decrease from *ca*. 50º–30º at the base to *ca*. 30º–10º a few hundred metres upsection and remain at comparable dips throughout the rest of the section (Fig. 9a). Further NE in SRb2, syn-rift strata dip between *ca*. 30º–10º throughout much of the section, although higher dips (up to 40º) are found within fault-bound slivers adjacent to the detachment (Fig. 9a). Yet, other regions of the basin clearly show an upsection decrease in bedding dips: at the base of SRb3 and Hb1, for example, dips range between *ca*. 35º–25º and *ca*. 25º–15º and decrease upsection to *ca*. 20º–5º and *ca*. 15º–5º, respectively (Fig. 9b). Likewise, bedding dips in the northeastern basin decrease from *ca*. 75º–45º at the base to *ca*. 45º–25º adjacent to the detachment (SRb4, SRb4 (W); Fig. 9b).

The simplest explanation for the apparent lack of a fanning dip section in the southwestern Santa Rosa basin would be that all tilting is solely due to domino-style block rotations that post-date deposition of the basin-fill. Post-depositional tilting of the basin would most likely have been associated with rotational faulting on the still active San Pedro Mártir fault further west. In this scenario, tilting of the basin cannot exceed the tilting experienced by the detachment footwall (mean of 10º towards W to NW based on field measurements and 3-point calculations). Thus, the maximum allowable amount of post-depositional tilting is 10º (assuming that all footwall tilting

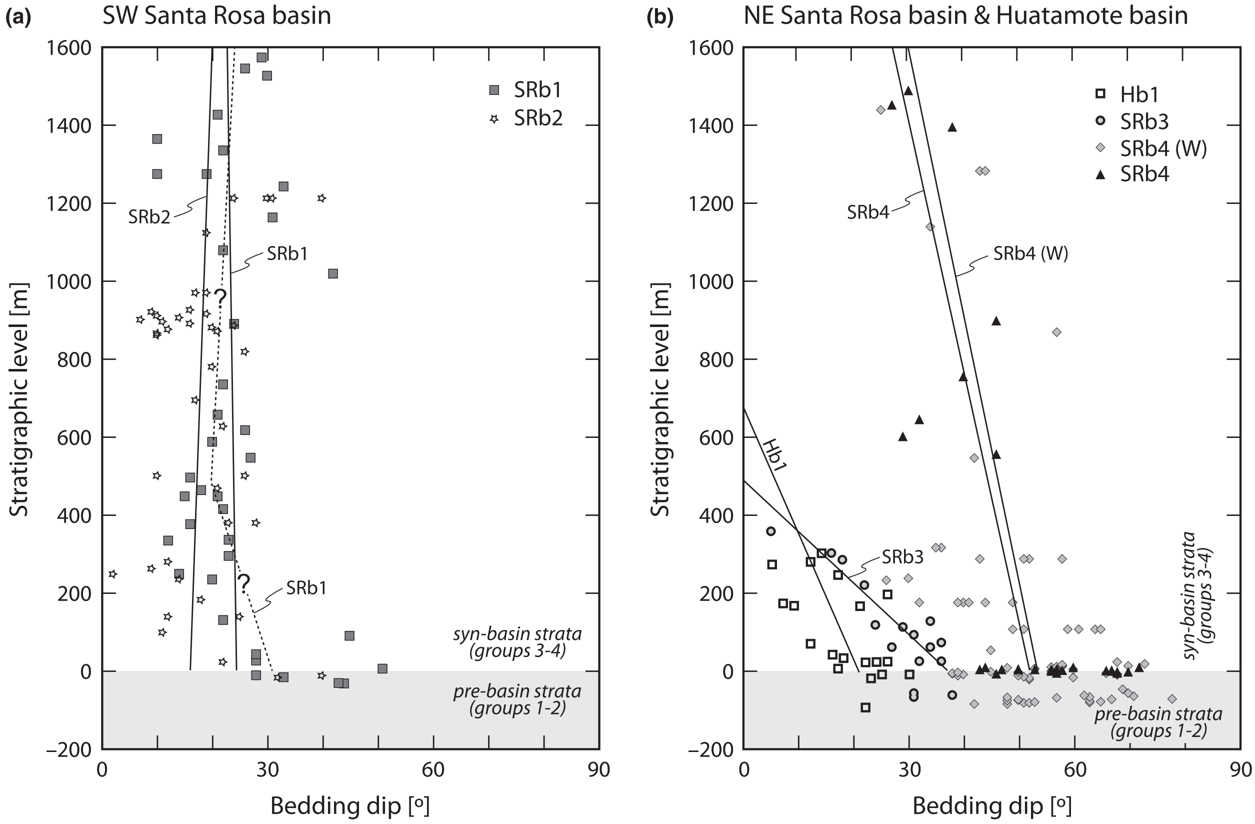

Fig. 9. Plot of bedding dip vs. stratigraphic level. a) Groups 3-4 strata of the southwestern Santa Rosa basin do not show a statistically significant trend of upsection shallowing, although there may be a fanning dip section in the early basin-fill of SRb1. b) Dips in the central to northeastern Santa Rosa basin and the northern Huatamote basin decrease with stratigraphic level as typical for a fanning dip sequence.

was post-depositional), which is significantly less than most measurements of the Santa Rosa basin. In the hanging wall of the detachment, group 1 and 2 strata dip *ca*. 25–30º more steeply than the corresponding units of the footwall (Figs 10 and 11). These relationships indicate that the Santa Rosa detachment is listric and imply that fault slip was rotational, which is also evident by a syntectonic rollover anticline that developed in the hanging wall (Figs 10 and 11; Seiler *et al.*, 2010). The resultant basin geometry is that of an asymmetric half-graben with a NW-ward thickening sedimentary wedge, which implies syndepositional tilting if sedimentation was coeval with fault slip as indicated by our data. This is consistent with the observed fanning of dips in the central and NE Santa Rosa basin as well as the northern Huatamote basin (SRb3-4, Hb1; Fig. 9b). Outcrop-scale sedimentological observations (e.g. slumping, asymmetric seismites) and predominantly hanging wall-derived sediment influx (including the Santa Rosa slide) further support the idea of syntectonic tilting in the Santa Rosa basin. In addition, the orientation of the basin fill is largely consistent with the extension direction of the corresponding detachment segment, which strongly suggests that tilting is linked to slip on the detachment (slip on the San Pedro Mártir fault is 40º more ENE than that of the Santa Rosa detachment; Stock & Hodges, 1990; Seiler *et al.*, 2010). Note that this syntectonic tilting occurred in addition to domino-style block rotations of up to 10º, which help explain the W- to NW-tilting of the detachment footwall, the relatively steep dip of the youngest basin-fill and the current low-angle orientation of the detachment.

LATERAL FACIES VARIATIONS ASSOCIATED WITH CONSTRICTIONAL STRAIN

Sediment dispersal in rift basins is primarily controlled by subsidence patterns and proximity to the uplifted neighbouring blocks. In a transverse section, rift basins commonly record three main types of depositional systems, consisting of colluvium and/or alluvial fans shed from the two basin margins and an axial depocentre facies of either lake/playa (internally draining) or fluvial (externally draining) deposits (e.g., Leeder & Gawthorpe, 1987; Gawthorpe & Leeder, 2000). Except for its NE part, the Santa Rosa basin has many characteristics that are compatible with the above facies model of extensional basins (Hb1-SRb3; Figs 10 and 11). In addition, the stratigraphy of the Santa Rosa basin reveals marked changes in grain size and lithofacies along the axis of the basin, suggesting that deposition was influenced by along-strike variations in structural boundary conditions (Figs 3, 10, 11).

Lateral facies variations on the scale of individual fan lobes can certainly be expected in an environment where different alluvial fans from variable source areas coalesce to form continuous deposits. However, at least two important changes in the facies architecture occur systematically across the entire Santa Rosa basin. First, the fine-grained depocentre facies first occurred in the central basin (SRb3) during the latest Miocene and developed progressively further upsection and thus later towards the SW basin (SRb1-2), where the detachment enters a broad synformal domain (Figs 3, 5, 10 and 11). The latest occurrence of the depocentre facies coincides approximately with the hinge of the major synformal corrugation of the Santa Rosa detachment, and the facies ends about 1 km north of the Amarillas transfer zone (Figs 3 and 5). Second, only the proximal (conglomeratic) fan facies developed in the NE Santa Rosa basin, which lies adjacent to a major antiformal detachment corrugation (Figs 3, 5, 10 and 11). Finite displacement on the Santa Rosa detachment is *ca*. 4–5 km and is similar along the entire NW basin margin (Figs 9 and 10; Seiler *et al.*, 2010). Thus, the observed differences in the basin-parallel facies architecture cannot be explained by differential footwall uplift due to along-strike slip gradients. Rather, the abundance of fine-grained facies in the synformal domain (SW) and the predominance of conglomerate near the antiformal corrugation (NE) suggest that the distribution of fine- and coarse-grained facies was at least partially controlled by syn-basinal growth of the fault corrugations. In addition, the detachment shape also modified the basin architecture, particularly near step-overs or transfer faults between different detachment strands (Fig. 2). Both mechanisms are consistent with sedimentological observations (e.g., palaeotransport, clast size, angularity and provenance), which are all indicative of short transport distances and a local source area.

Large-scale, extension-parallel corrugations are commonly found on detachment faults and may form as (a) original fault corrugations (e.g., Spencer, 1985; John, 1987), (b) displacement gradient folds that develop due to differential isostatic rebound of the footwall (e.g., Schlische, 1993, 1995), or (c) syntectonic constrictional folding orthogonal to the extension direction (e.g., Yin & Dunn, 1992; Mancktelow & Pavlis, 1994). All three of the above end-member processes likely contributed to shape the Santa Rosa detachment. However, several independent lines of evidence suggest that extension-parallel N-S constrictional folding, itself an integral part of the transtensional strain regime of the oblique plate boundary, was probably the dominant driving force. Structural analysis by Seiler *et al.* (2010) revealed that open upright folds trending ESE-WNW affected both the detachment fault and the basin-fill of the Santa Rosa basin, with fold axes and axial surfaces that are compatible between the two (Fig. 2). The degree of folding in the detachment corrugations and the pre-tectonic strata of groups 1 and 2 is comparable and significantly more than in latest Miocene to Late Pliocene-Pleistocene (groups 3 and 4) strata, implying that N-S constrictional folding began early during detachment faulting (Seiler *et al.*, 2010). Low-temperature thermochronology further indicates a strongly SW-ward decreasing gradient in

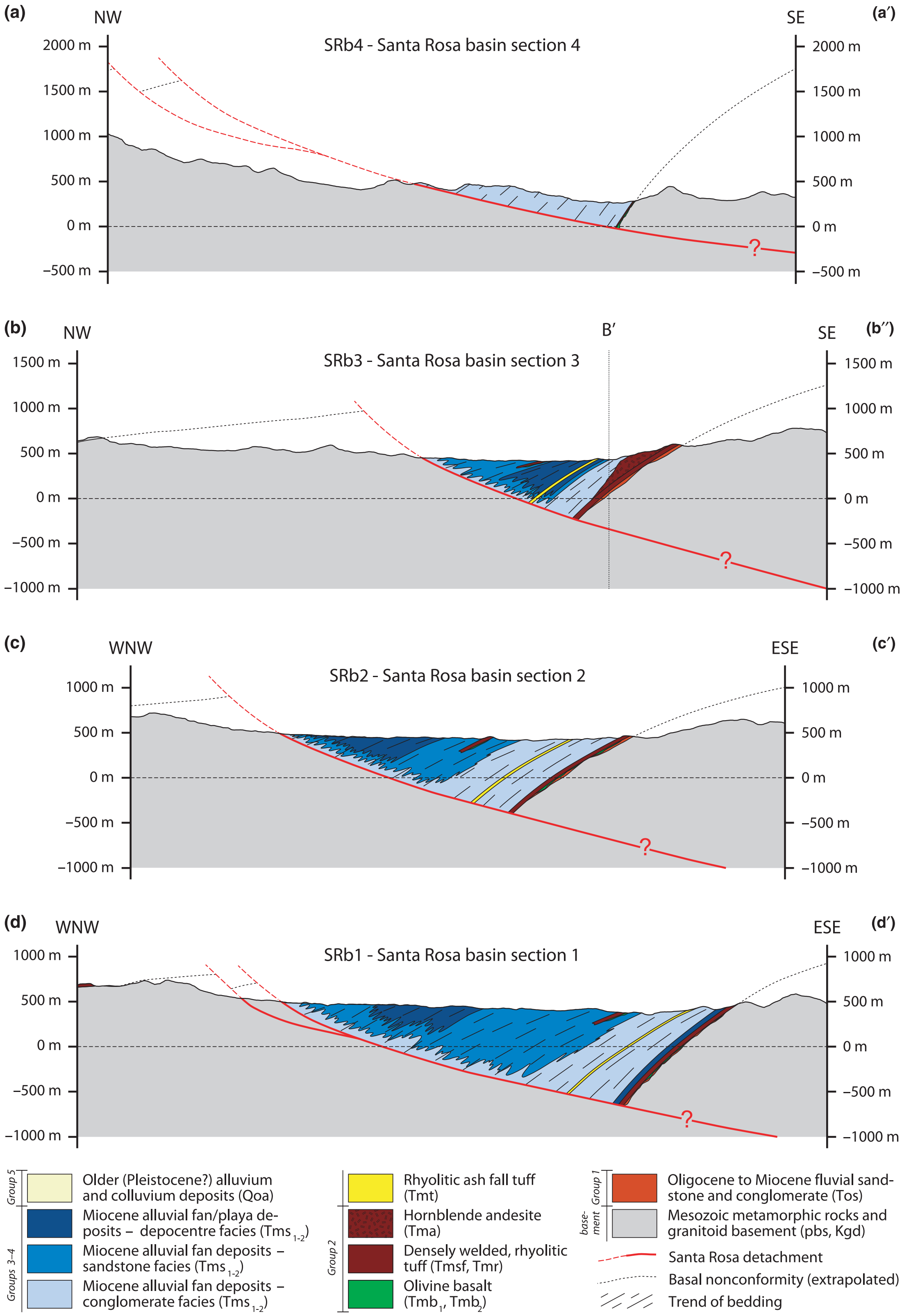

Fig. 10. Serial cross sections across the Santa Rosa basin showing lateral and across-basin facies variations. Section locations are shown in Fig. 5.

footwall exhumation along the Santa Rosa basin, from *ca.* 2.5 km near the antiformal hinge to <0.5 km in the synform axis (Seiler *et al.*, 2011). Given that finite displacement was largely comparable over the same area (Figs 10 and 11), the observed differences in footwall exhumation most likely represent vertical deflections (uplift/subsidence) associated with upright N-S constrictional folding (Seiler *et al.*, 2011).

The facies relationships reported here are clearly consistent with the vertical deflections predicted by extension-parallel constrictional folding. In this interpretation, the upward motion associated with antiformal folding led to sustained uplift in both foot and hanging wall, which resulted in steep topographic gradients and a high influx of coarse detritus into the northeastern Santa Rosa basin (Figs 10 and 11). By contrast, the downward deflection of the synformal domain resulted in increased subsidence and the development of a well-established depocentre in the southwestern basin, consistent with the observed southwestward migration of the depocentre through time (Figs 5, 10 and 11). These relationships are also consistent with the present-day relief, which is highest in the footwall of the antiformal domain and lowest in the area of the synform axis (Figs 9 and 10; Seiler *et al.*, 2011).

The influence of the detachment fault shape on the basin architecture is best shown in the NE Santa Rosa basin (Fig. 2). The thick stratigraphic section in SRb4 may at first seem inconsistent with our interpretation of increased uplift in an antiformal hinge (Figs 2 and 3). Figure 2 shows that SRb4 is located in a step-over between two detachment strands SW of the antiformal hinge, where an original fault asperity provides additional accommodation space for the basin-fill. The sinistral-oblique motion of the step-over segment (Seiler *et al.*, 2010) also produced significant fault drag in the hanging wall strata (Fig. 2), which resulted in a contorted section line that increases the effective stratigraphic thickness of SRb4. Thus, both the shape and kinematics of the detachment influenced the observed basin architecture at this location. In addition, exposed crustal levels in the NE are deeper and closer to the underlying detachment than elsewhere in the basin and as a result, the section appears thicker due to the fanning geometry of the half-graben fill here (Figs 9–11). Closer to the anticline, the basin pinches out and there is no hanging wall basin preserved in the actual hinge zone as predicted by our model (Fig. 2).

Despite their obvious influence on the geometry of the Santa Rosa basin (Fig. 2), it is difficult to evaluate how important transfer faults are with respect to the observed facies patterns. The Amarillas transfer zone illustrates this point: it obviously had a major influence on the basin geometry as its southern structural boundary (Fig. 2) and yet, appears to have had little impact on the facies in terms of grain size, although there are differences in clast provenance and palaeotransport. This may be due to the unique location of the Santa Rosa basin along the transfer fault, which changes from dextral (W) to sinistral (E) at this location (Fig. 2), implying that both fault slip and topographic gradients were minor (Seiler *et al.*, 2010). In any case, only a major structural feature operating on the scale of the detachment can explain the observed basin-wide lateral facies variations (e.g., the SW migration of the depocentre with time and SW-ward decrease in grain size) and account for differential footwall exhumation recorded by low-temperature thermochronology (i.e., Seiler *et al.*, 2011). We conclude that N-S constrictional folding of the Santa Rosa detachment exerts a primary control on the along-strike facies variations of the Santa Rosa basin, although step-overs and transfer faults also had a significant influence on the basin geometry as local structural boundaries.

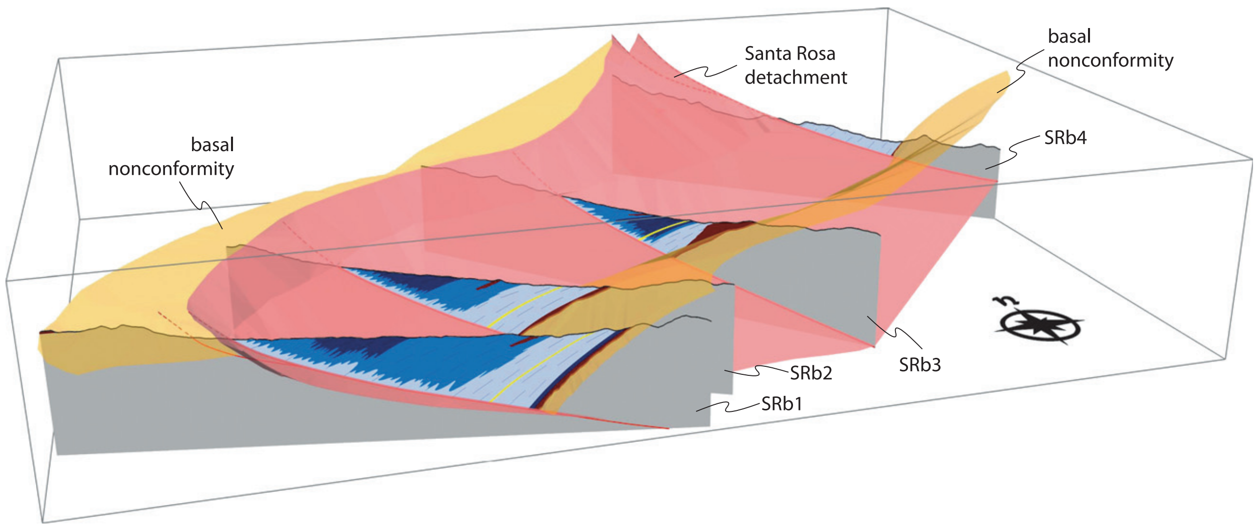

Fig. 11. Block diagram of the Santa Rosa basin based on the serial cross sections of Fig. 10. Group 1 and 2 deposits are collectively shown in brown, colours of other rock units and facies associations are the same as in Fig. 10. The listric Santa Rosa detachment (red transparent surface) is the basin-bounding master fault that dips shallowly SE-ward below the Santa Rosa basin. Fault displacement across the Santa Rosa detachment is largely similar along the length of the basin, as shown by comparable offsets of the NW-tilted Oligocene unconformity (orange transparent surface) throughout the Santa Rosa basin. Relief is highest in the northeastern part of the basin (SRb4; see also Fig. 10), where the stratigraphy is dominated by coarse clastic sedimentation and the detachment fault is at relatively shallow crustal levels, which is likely due to increased uplift and erosion in the antiformal hinge region. By comparison, increased subsidence in the synformal hinge zone led to the migration of the depocentre from the central Santa Rosa basin (SRb3) to the southwestern basin (SRb1-2) during the latest Miocene and Pliocene.

It is these along-strike facies variations that define the Santa Rosa basin as a transtensional basin, because they are largely formed by constrictional folding. Such folding, by definition, occurs in response to horizontal shortening perpendicular to the extension direction and is an integral part of transtensional shearing. Thus, the transtensional character of the Santa Rosa basin differs substantially from other transtensional basins and demonstrates that such basins need not be bounded by linked sets of normal and strike-slip faults. Rather, significant wrenching can be accommodated by distributed deformation associated with syndepositional macroscopic folding of the basin and its bounding normal fault. This represents a new type of transtensional basin, here named *constrictional rift basin*, that forms in settings where oblique extension is partitioned between distributed extension-perpendicular shortening (strike-slip component) and discrete normal faulting (extensional component).

Another basin where lithofacies variations are associated with constrictional folding is the Miocene north Whipple basin above the Whipple detachment in western Arizona (Dorsey & Roberts, 1996). Like the Santa Rosa basin, the north Whipple basin shows two orthogonal axes of tilting that influence the facies architecture of the basin: one perpendicular to the extension direction associated with the formation of a fault-bound half graben, and one parallel to the extension direction likely resulting from the growth of extension-parallel folds in the detachment surface (Dorsey & Roberts, 1996). In both basins, deposition near the antiformal hinge is dominated by coarse clastics shed from the high-standing topography of the antiform, and the thickest stratigraphic section accumulated in the region of maximum subsidence around the synform axis. However, there are significant differences in the facies architecture that are associated with the different tectonic settings of the basins. Finite slip on the Whipple detachment far exceeds displacement on the Santa Rosa detachment (*ca*. 40 km vs. *ca*. 4–5 km; Davis & Lister, 1988; Seiler *et al.*, 2010). Yet, the amplitude of constrictional folding of the Whipple detachment – at the scale that affected the north Whipple basin – was much less (*ca*. 200 –400 m vs. *ca*. 4 km; Yin & Dunn, 1992; Seiler *et al.*, 2010), and folding was asymmetric (Dorsey & Roberts, 1996). As a result, the north Whipple basin-fill exhibits distinctly different characteristics. The primary source region was the detachment footwall, and along-axis sediment transport was significant (Dorsey & Roberts, 1996). The asymmetric style of folding resulted in the accumulation of a thick section of conglomerate along the synform axis, shed directly from the antiformal bulge of the nearby Whipple mountains further south (Dorsey & Roberts, 1996). Perhaps surprizingly, a second anticline in the northern section of north Whipple basin coincides with fine-grained sedimentation in a distal low-energy fluvial or lacustrine environment (Dorsey & Roberts, 1996), which may be due to the fact that this anticline is superimposed on a larger-scale syncline separating the domal bulges of the Whipple and Chemehuevi mountains.

These differences show that lateral facies variations associated with vertical deflections are strongly dependent on the local setting of the basins, and cannot easily be generalized into a universal stratigraphic model. However, most of the sedimentological differences between the Santa Rosa and North Whipple basins are simply due to the fact that, in a transverse direction, the former is a hybrid rift-supradetachment basin (see below), whereas the latter is a simple supradetachment basin. We propose that constrictional rift basins will have the following key stratigraphic elements: 1) syn-depositional extension-parallel folding of basin strata, 2) basin-parallel grain size gradients that can be related to the wave length of extension-parallel folds, 3) strong influx of coarse clastics and limited subsidence near the high-standing antiform and 4) maximum subsidence near the synform axis, perhaps associated with the progressive migration of maximum subsidence towards the synform region. In addition, the bounding fault of a constrictional rift basin more likely has a low-angle inclination with potentially complex fault kinematics, antiformal and/or synformal megamullions and gradients in footwall exhumation that are coupled with megamullion wave length.

BASIN EVOLUTION

We propose the following model for the evolution of the Santa Rosa basin: Deposition of the syntectonic strata of the Santa Rosa basin occurred in a constrictional rift basin in the upper plate of the Santa Rosa detachment (Fig. 11), in an environment that was either arid or semi-arid. Although the basin formed above a detachment fault, it has characteristics of both supradetachment basins (corrugated low-angle bounding fault, ridge & swale topography in footwall, footwall uplift > subsidence [in NE], basin fill dominated by conglomerate and megabreccia [in NE]), and 'traditional' rift basins (high initial fault angle [*ca*. 55–60°; Seiler *et al.*, 2010], moderate slip rates and displacement, subsidence > footwall uplift [in SW], hanging wall dominated sediment influx with depocentres proximal to the bounding fault).

Faulting on the detachment initiated at *ca*. 9 Ma approximately mid-way between the (present-day) antiformal and synformal corrugations, and led to the deposition of a footwall-derived alluvial/colluvial megabreccia in the central Santa Rosa basin. Syntectonic sedimentation in the NE basin began shortly after and resulted in the development of a small but significant angular unconformity within the lowest group 3 strata. At that time, the SW basin was still outside the area of active faulting and experienced lacustrine(?) to distal fan delta deposition in a pre-existing surface depression.

The Santa Rosa detachment, at this stage still a high-angle normal fault, grew rapidly along-strike and reached its present-day strike-length before *ca*. 7 Ma (i.e. before deposition of the 6.78 Ma ash fall tuff). Rapid subsidence in the central Santa Rosa basin, which lies adjacent to the oldest and best developed section of detachment, led to the establishment of a depocentre that became filled with fine-grained fan delta and playa deposits (Figs 5 and 10). Elsewhere in the basin, sediment dispersal occurred on the tilted slopes of sheetflood-dominated alluvial fans, which traversed the basin from both hanging wall and footwall. Differential folding between the pre-rift strata (groups 1–2), the early basin-fill (group 3) and late syntectonic deposits (group 4) conclusively shows that N-S constrictional strain began folding the detachment and basin-fill at this stage (Seiler *et al.*, 2010). At 6.78 Ma, eruption of rhyolitic magma from a nearby vent led to the deposition of the ash fall tuff (Tmt), which provides an important snapshot of the various depositional environments that were active at the time (Fig. 11).

Subsidence in the southwestern Santa Rosa basin peaked during the latest Miocene to Early Pliocene (after 6.78 Ma) and led to the lateral expansion of the depocentre facies (Fig. 11). SE of the basin axis, the depocentre shows a gradual transition from playa and fan delta to distal alluvial fans shed from the hanging wall in the Sierra Santa Rosa (Fig. 11). By contrast, the NW boundary of the depocentre is constrained by laterally interfingering alluvial fans that prograded SE from the footwall (Fig. 11). Progressive tilting of the Sierra Santa Rosa, partially associated with the formation of a rollover anticline above the listric Santa Rosa detachment, resulted in a large areal exposure of group 2 volcanics on a tilted slope. Sometime after 6.78 Ma, an earthquake probably triggered the detachment of a large slide sheet comprising the Early Miocene basalt and the Tuff of San Felipe, which moved *ca*. 1–3 km downslope and became fragmented into several internally coherent blocks.

Throughout the latest Miocene and Pliocene, the corrugations of the detachment and the corresponding folds in the basin-fill were further amplified by constrictional folding, reflecting the sustained transtensional strain regime of the plate boundary. This folding caused broad uplift in the antiformal hinge in the NE of the study area, affecting both the footwall and hanging wall. In the latter, uplift was partially or fully compensated by subsidence associated with fault slip on the detachment, thereby providing the accommodation space to facilitate further deposition. The combination of steep topographic gradients and a short transport distance in the antiformal hinge zone readily explains the predominance of coarse conglomerate and the lack of the depocentre facies in the NE basin (Fig. 11). By contrast, the synformal domain in the SW basin experienced substantially higher subsidence rates because the downward motion of the syncline was superimposed on fault-related subsidence (Fig. 11). This resulted in a gradual southwestward migration of the main depocentre into the synformal domain after 6.78 Ma.

In addition to constrictional folding, the entire Santa Rosa basin probably also experienced vertical-axis block rotations similar to those found further south (Fig. 1; Lewis & Stock, 1998b). Palaeomagnetic data indicate that the northern Huatamote basin (Hb1) experienced *ca*. 41° of clockwise rotation since deposition of the Tuff of San Felipe at *ca*. 12.6 Ma (Fig. 1; Stock *et al.*, 1999), although the exact onset and duration of these rotations is unclear (see discussion in Seiler *et al.*, 2010). Unfortunately, no palaeomagnetic data are available from anywhere north of the Amarillas transfer zone, and further studies are necessary to 1) refine the amount and timing of any vertical-axis rotations in the Santa Rosa basin, and 2) define whether the corrugations developed as symmetric or asymmetric folds.

At some poorly constrained time during the latest Pliocene(?) or Pleistocene, slip rates decreased and faulting on the Santa Rosa detachment ceased. A certain amount of tilting and erosion affected the Santa Rosa basin-fill at a late to post-depositional stage and is documented by a marked angular unconformity between the NW-dipping strata of group 4 and subhorizontal alluvial fan deposits of group 5, which prograded from the footwall across the Santa Rosa basin during the Late(?) Quaternary (Fig. 4d). It is possible that once slip had ceased on the Santa Rosa detachment, both foot and hanging wall behaved as a single coherent block in the hanging wall of the listric San Pedro Mártir fault, which likely forms a regional detachment horizon at depth. Late Quaternary fault scarps suggest recent or ongoing activity on the San Pedro Mártir fault (Brown, 1978), implying that the break-away fault outlasted the Santa Rosa detachment. It is thus likely that continued rotational deformation in the hanging wall of the San Pedro Mártir was responsible for further tilting (up to *ca*. 10°) of the basin-fill after slip on the basin-bounding detachment had ceased.

CONCLUSIONS

Sedimentary rocks exposed in the Santa Rosa basin accumulated in a transtensional basin in the hanging wall of the top-to-the-southeast Santa Rosa detachment during oblique rifting in the Gulf of California. The syn-rift stratigraphy displays systematic basin-scale variations in the facies architecture both along-strike and across the axis of the basin. Boulder conglomerate and breccia at the base of the section were deposited as proximal alluvial fans and rock avalanches in the piedmont zone of the incipient detachment. These deposits are interbedded between two volcanic units that bracket the initiation of faulting between 9.36 ± 0.14 Ma and 6.78 ± 0.12 Ma. In the central and southwestern Santa Rosa basin, the basin-fill exhibits an overall fining-upward cycle that culminates in interbedded sandstone and mudstone representing the distal fan delta and playa facies of the depocentre. These deposits interfinger laterally with coarse sandstone and conglomerate of the proximal alluvial fan and fault-scarp facies that originated in the footwall and traversed southeastward across the basin. In the northeastern basin, the finer grained facies is not developed and the sequence is dominated by conglomerate and breccia. Clast provenance and palaeoflow directions indicate that sediment dispersal was transverse-dominated, strongly event-controlled and occurred on mostly low-gradient alluvial fans from catchments in the footwall and/or hanging wall of the detachment.

Facies patterns also vary parallel to the basin axis, despite the fact that finite displacement was comparable along the basin margin. Two key observations are: (a) the depocentre facies developed progressively later towards the southwestern Santa Rosa basin, and (b) only the proximal fan facies developed in the northeastern part of the basin. The differences in the lateral facies architecture are linked with major synformal and antiformal corrugations of the detachment fault, respectively, which formed as extension-parallel upright folds during the N-S constrictional strain regime of the oblique plate boundary. The upward vertical deflection caused by antiformal buckling led to increased uplift in both foot and hanging wall, thereby choking the northeastern basin with conglomerate and breccia. By comparison, the downward deflection of the synformal domain produced increased subsidence there, which resulted in the southwestward migration and progressive localization of the depocentre in the synformal hinge zone. Thus, the Santa Rosa basin is an example of a constrictional rift basin, a new type of transtensional basin in which oblique-divergent shear was partitioned between normal faulting on discrete fault zones and distributed constrictional strain that was accommodated by folding of the rock volume.

The $^{40}Ar/^{39}Ar$ dating of two volcanic units that are apparently intercalated within the syntectonic basin-fill yielded Early to Middle Miocene ages that duplicate the ages of pre-rift volcanic rocks. Given their similarity in appearance and age, they are interpreted as allochthonous, gravity-driven slide block deposits that detached from the moderately tilted hanging wall (<16º) sometime after 6.78 Ma. During emplacement, which was likely triggered by an earthquake, the slide sheet fragmented into a number of internally coherent blocks that moved between *ca*. 1–3 km down-hill on the active depositional environment of shallowly basin-ward dipping alluvial fans.

APPENDIX ^{40}AR/^{39}AR ANALYTICAL DETAILS

Mineral samples were prepared using standard crushing, sieving, magnetic and heavy liquid separation techniques. To minimize the risk of contamination from lithic fragments, samples were screened after the crushing stage (1–2 cm diameter) and only lithic-free chips were processed further. Sanidine, hornblende, plagioclase and biotite separates were handpicked to >99% purity. Whole rock samples were crushed, washed, sieved to chips of 180–250 μm, and handpicked to minimize the risk of argon loss or excess argon associated with alteration, vesicles and/or phenocrysts. All separates were immersed in 4% HCl and 4% HNO_3 for 10 min to dissolve secondary carbonate and rinsed thoroughly with deionized water in an ultrasonic bath. Separates were weighed, packed into aluminium foil packets, loaded in quartz tubes along with five interspersed aliquots of the neutron fluence monitor GA1550 (98.79 ± 0.96 Ma; Renne *et al.*, 1998) and irradiated for 13:20 h in position 5c (cadmium-lined) of the McMaster University reactor in Hamilton, Canada.

Irradiated samples and standards were analysed in the $^{40}Ar/^{39}Ar$ laboratory of the School of Earth Sciences, University of Melbourne, following procedures described previously by Phillips *et al.* (2007) and Matchan & Phillips (2011). GA1550 biotite standard grains were fused with a Nd-YAG laser and analysed on a VG5400 mass spectrometer equipped with a Daly detector, following gas purification by three Zr-Al getters. Analyses of purified air aliquots from a calibrated pipette yielded a mass discrimination factor of 1.0049 ± 0.22 amu^{-1} for this system. Multigrain aliquots of irradiated samples were packed in tin foil and step-heated in a double vacuum tantalum resistance furnace. The extracted gas was purified by Zr-Al getters and analysed using a VG3600 mass spectrometer and Daly detector. Mass discrimination for this system was calculated at 1.0075 ± 0.0016 amu^{-1} relative to an atmospheric $^{40}Ar/^{36}Ar_{atm}$ ratio of 295.5 ± 0.5 (Steiger & Jaeger, 1977). Different protocols were employed for the standards and the samples due to the unavailability of a laser system on the VG3600.

Reported argon isotope abundances have been corrected for system blanks, mass discrimination, radioactive decay and, in case of $^{40}Ar^*$, nuclear interference reactions. Decay constants used are those of Steiger & Jaeger (1977). Correction factors for interfering isotope reactions are $(^{36}Ar/^{37}Ar)_{ca} = 2.89 \pm 0.05 \times 10^{-4}$, $(^{39}Ar/^{37}Ar)_{Ca} = 6.80 \pm 0.20 \times 10^{-4}$, $(^{40}Ar/^{39}Ar)_K = 4.0 \pm 4.0 \times 10^{-4}$, $(^{38}Ar/^{39}Ar)_K = 1.3 \pm 0.5 \times 10^{-2}$. Apparent age spectra and inverse isochron diagrams were plotted using Isoplot v3.71 (Ludwig, 2008). Plateau ages are defined as incorporating three or more contiguous steps with no resolvable slope (at 95% confidence levels) that together comprise >50% of the total ^{39}Ar released and show step-release ages that overlap with the weighted mean age at 2σ levels. Inverse isochron regressions were calculated using the plateau segment steps and are shown in Supplementary Fig. S2. All inverse isochron plots reveal a trapped argon component ($^{40}Ar/^{36}Ar_i$) that is within error of the atmospheric $^{40}Ar/^{36}Ar_{atm}$ ratio (Fig. S2; Table 5). In many cases, data points cluster within a narrow range on the inverse isochron diagrams, resulting in larger uncertainties in inverse isochron ages when compared with plateau ages (Figs 8, S2). For this reason, we prefer plateau ages over inverse isochron ages, and although both are reported in Table 5, we only discuss plateau ages in the text.

ACKNOWLEDGEMENTS

This research was supported by ARC grants DP06651274 and DP1092861 to AG and BK, and by CONACYT grant #81463 and NSF EAR-0739017 Sub-Award 08-004375-

01 to JF. The $^{40}Ar/^{39}Ar$ laboratory at the University of Melbourne receives infrastructure support under the AuScope Program of NCRIS. We thank Yvonne Kunz for the invaluable support and assistance in the field and Stanislav Szczepanski for technical assistance in the $^{40}Ar/^{39}Ar$ lab. The paper benefited from careful and constructive reviews by Rebecca Dorsey, Paul Umhoefer and Emmanuel Masini and editorial oversight by Peter van der Beek.

SUPPORTING INFORMATION

Additional Supporting Information may be found in the online version of this article:

Figure S1. Detailed stratigraphic sections of the Santa Rosa basin.

Figure S2. Inverse isochron diagrams for samples from the Santa Rosa basin. Errors are given as $\pm 1\sigma$ unless otherwise stated.

Table S1. $^{40}Ar/^{39}Ar$ Furnace step-heating analytical data

Table S2. Furnace blank measurements

Please note: Wiley-Blackwell are not responsible for the content or functionality of any supporting materials supplied by the authors. Any queries (other than missing material) should be directed to the corresponding author for the article.

REFERENCES

Anders, M.H., Aharonov, E. & Walsh, J.J. (2000) Stratified granular media beneath large slide blocks; implications for mode of emplacement. *Geology*, **28**, 971–974.

Andersen, R.L. (1973) *Geology of the Playa San Felipe Quadrangle, Baja California, Mexico*. MSc Thesis, California State University San Diego, San Diego.

Anderson, P.V. (1993) Prebatholithic stratigraphy of the San Felipe area, Baja California Norte, Mexico. In: *The prebatholithic stratigraphy of Peninsular California*. *Geol. Soc. Am. Spec. Pap.* (Ed. by Gastil R.G. & Miller R.H.) **279**, 1–10.

Atwater, T. (1970) Implications of plate tectonics for the Cenozoic tectonic evolution of western North America. *Geol. Soc. Am. Bull.*, **81**, 3513–3535.

Atwater, T. & Stock, J.M. (1998) Pacific-North America plate tectonics of the Neogene southwestern United States: An update. *International Geology Review*, **40**, 375–402.

Black, N. (2004) *Structure and Hanging Wall Stratigraphy of the Las Cuevitas Detachment, Central Sierra San Felipe, Baja California, Mexico*. MSc Thesis, University of California Los Angeles, Los Angeles.

Blair, T.C. & McPherson, J.G. (1994) Alluvial fans and their natural distinction from rivers based on morphology, hydraulic processes, sedimentary processes, and facies assemblages. *J. Sediment. Res.*, **64**, 450–489.

Boehm, M.C. (1984) An overview of the lithostratigraphy, biostratigraphy, and paleoenvironments of the late Neogene San Felipe marine sequence, Baja California Sur, Mexico. *Field Trip Guidebook - Pacific Section, Society of Economic Paleontologists and Mineralogists*, **39**, 253–265.

Bosworth, W., Huchon, P. & McClay, K. (2005) The Red Sea and Gulf of Aden basins. *J. Afr. Earth Sc.*, **43**, 334–378.

Boyer, S.E. & Hossack, J.R. (1992) Structural features and emplacement of surficial gravity-slide sheets, northern Idaho-Wyoming thrust belt. *Memoir - Geological Society of America*, **179**, 197–213.

Brown, L.G. (1978) *Recent Fault Scarps Along the Eastern Escarpments of the Sierra San Pedro Mártir, Baja California*. MSc Thesis, San Diego State University, San Diego.

Bryant, B.A. (1986) *Geology of the Sierra Santa Rosa basin, Baja California, Mexico*. MSc Thesis, San Diego State University, San Diego.

Bull, W.B. (1972) Recognition of alluvial-fan deposits in the stratigraphic record. *Special Publication - Society of Economic Paleontologists and Mineralogists*, **16**, 63–83.

Bull, W.B. (1977) The alluvial-fan environment. *Prog. Phys. Geogr.*, **1**, 222–270.

Cope, T., Luo, P., Zhang, X.Y., Zhang, X.J., Song, J.M., Zhou, G. & Shultz, M.R. (2010) Structural controls on facies distribution in a small half-graben basin: Luanping basin, northeast China. *Basin Res.*, **22**, 33–44.

Davies, S.J., Dawers, N.H., McLeod, A.E., Underhill, J.R., Gupta, S. & Cowie, P.A. (2000) The structural and sedimentological evolution of early synrift successions; the Middle Jurassic Tarbert Formation, North Sea. *Basin Res.*, **12**, 343–365.

Davis, G.A. & Friedmann, S.J. (2005) Large-scale gravity sliding in the Miocene Shadow Valley supradetachment basin, eastern Mojave Desert, California. *Earth Sci. Rev.*, **73**, 149–176.

Davis, G.A. & Lister, G.S. (1988) Detachment faulting in continental extension: Perspectives from the Southwestern U.S. Cordillera. *Geol. Soc. Am. Spec. Pap.*, **218**, 133.

Dokka, R.K. & Merriam, R.H. (1982) Late Cenozoic extension of northeastern Baja California, Mexico. *Geol. Soc. Am. Bull.*, **93**, 371–378.

Dorsey, R.J. & Burns, B. (1994) Regional stratigraphy, sedimentology, and tectonic significance of Oligocene-Miocene sedimentary and volcanic rocks, northern Baja-California, Mexico. *Sed. Geol.*, **88**, 231–251.

Dorsey, R. & Martin-Barajas, A. (1999) Sedimentation and deformation in a Pliocene-Pleistocene transtensional supradetachment basin, Laguna Salada, north-west Mexico. *Basin Res.*, **11**, 205–221.

Dorsey, R.J. & Roberts, P. (1996) Evolution of the Miocene North Whipple Basin in the Aubrey Hills, western Arizona, upper plate of the Whipple detachment fault. *Geological Society of America Special Papers*, **303**, 127–146.

Dorsey, R.J. & Umhoefer, P.J. (2012) Influence of sediment input and plate-motion obliquity on basin development along an active oblique-divergent plate boundary: Gulf of California and Salton Trough. In: *Tectonics of Sedimentary Basins: Recent Advances* (Ed. by C. J. Busby & A. Azor Pérez), 209–225. Blackwell Publishing, Chichester, UK.

Esser, R.P. & McIntosh, W.C. (2003) *40Ar/39Ar Geochronology Results from the Bay of Los Angeles*. Baja, Mexico, New Mexico Bureau of Geology and Mineral Resources. 25.

Fletcher, J.M. & Mungúia, L. (2000) Active continental rifting in southern Baja California, Mexico: Implications for plate motion partitioning and the transition to seafloor spreading in the Gulf of California. *Tectonics*, **19**, 1107–1123.

Fletcher, J.M. & Spelz, R.M. (2009) Patterns of Quaternary deformation and rupture propagation associated with an active low-angle normal fault, Laguna Salada, Mexico; Evidence of a rolling hinge? *Geosphere*, **5**, 385–407.

Fletcher, J.M., Grove, M., Kimbrough, D., Lovera, O. & Gehrels, G.E. (2007) Ridge-trench interactions and the Neogene tectonic evolution of the Magdalena Shelf and southern Gulf of California: Insights from detrital zircon U-Pb ages from the Magdalena Fan and adjacent areas. *Geol. Soc. Am. Bull.*, **119**, 1313–1336.

Friedmann, S.J. (1997) Rock-avalanche elements of the Shadow Valley basin, eastern Mojave Desert, California: Processes and problems. *J. Sediment. Res.*, **67**, 792–804.

Friedmann, S.J. & Burbank, D.W. (1995) Rift basins and supradetachment basins: Intracontinental extensional end-members. *Basin Res.*, **7**, 109–127.

Gastil, R.G., Lemone, D.V. & Stewart, W.J. (1973) Permian Fusulinids from near San Felipe, Baja California. *Am. Assoc. Pet. Geol. Bull.*, **57**, 746.

Gastil, R.G., Phillips, R.P. & Allison, E.C. (1975) *Reconnaissance geology of the State of Baja California*. *Geol. Soc. Am. Mem.*, **140**.

Gastil, R.G., Krummenacher, D. & Minch, J. (1979) The record of Cenozoic volcanism around the Gulf of California. *Geol. Soc. Am. Bull.*, **90**, 839–857.

Gawthorpe, R.L. & Leeder, M.R. (2000) Tectono-sedimentary evolution of active extensional basins. *Basin Res.*, **12**, 195–218.

González-Fernández, A., Dañobeitia, J.J., Delgado-Argote, L.A., Michaud, F., Córdoba, D. & Bartolomé, R. (2005) Mode of extension and rifting history of upper Tiburón and upper Delfin basins, northern Gulf of California. *J. Geophys. Res.*, **110**, B01313.

Gupta, S., Underhill, J.R., Sharp, I.R. & Gawthorpe, R.L. (1999) Role of fault interactions in controlling synrift sediment dispersal patterns; Miocene, Abu Alaqa Group, Suez Rift, Sinai. Egypt. *Basin Res.*, **11**, 167–189.

Hamilton, W.B. (1971) Recognition on space photographs of structural elements of Baja California. Professional Paper, U. S. Geological Survey. **718**, 26.

Hausback, B.P. (1984) Cenozoic volcanic and tectonic evolution of Baja California Sur, Mexico. *Field Trip Guidebook - Pacific Section, Society of Economic Paleontologists and Mineralogists*, **39**, 219–236.

Janecke, S., McIntosh, W. & Good, S. (1999) Testing models of rift basins: Structure and stratigraphy of an Eocene-Oligocene supradetachment basin, Muddy Creek half graben, south-west Montana. *Basin Res.*, **11**, 143–165.

John, B.E. (1987) Geometry and evolution of a mid-crustal extensional fault system: Chemehuevi Mountains, southeastern California. In: *Continental Extensional Tectonics*. *Geol. Soc. Spec. Pup.* (Ed. by M. P. Coward, J. F. Dewey & P. L. Hancock), **28**, 313–335.

Kimbrough, D.L., Smith, D.P., Mahoney, J.B., Moore, T.E., Grove, M., Gastil, R.G., Ortega-Rivera, A. & Fanning, C.M. (2001) Forearc-basin sedimentary response to rapid Late Cretaceous batholith emplacement in the Peninsular Ranges of southern and Baja California. *Geology*, **29**, 491–494.

Klitgord, K.D., Mudie, J.D., Bischoff, J.L. & Henyey, T.L. (1974) Magnetic Anomalies in the Northern and Central Gulf of California. *Geol. Soc. Am. Bull.*, **85**, 815–820.

Lee, J., Miller, M.M., Crippen, R., Hacker, B. & Vazquez, J.L. (1996) Middle Miocene extension in the Gulf Extensional Province, Baja California: Evidence from the southern Sierra Juarez. *Geol. Soc. Am. Bull.*, **108**, 505–525.

Leeder, M.R. & Gawthorpe, R.L. (1987) Sedimentary models for extensional tilt-block/half-graben basins. *Geol. in:Continent Extensional Tectonics. Soc. Am. Spec. Pup.* (Ed. by M. P. Coward, J. F. Dewey & P. L. Hancock) , **28**, 139–152.

Lewis, C.J. (1996) Stratigraphy and geochronology of Miocene to Pliocene volcanic and marine rocks in the Sierra San Fermín and southern Sierra San Felipe, Baja California, Mexico. *Geofísica Internacional*, **35**, 3–25.

Lewis, C.J. & Stock, J.M. (1998a) Late Miocene to Recent transtensional tectonics in the Sierra San Fermín, northeastern Baja California, Mexico. *J. Struct. Geol.*, **20**, 1043–1063.

Lewis, C.J. & Stock, J.M. (1998b) Paleomagnetic evidence of localized vertical axis rotation during Neogene extension, Sierra San Fermín, northeastern Baja California, Mexico. *J. Geophys. Res.*, **103**, 2455–2470.

Ludwig, K.R. (2008) *User's Manual for Isoplot 3.6, a Geochronological Toolkit for Microsoft Excel*. Berkeley Geochronology Center Special Publications, Berekeley. **4**, 77p.

Mack, G.H. & Stout, D.M. (2005) Unconventional distribution of facies in a continental rift basin; the Pliocene-Pleistocene Mangas Basin, south-western New Mexico, USA. *Sedimentology*, **52**, 1187–1205.

Mack, G.H., Seager, W.R., Leeder, M.R., Perez-Arlucea, M. & Salyards, S.L. (2006) Pliocene and Quaternary history of the Rio Grande, the axial river of the southern Rio Grande rift, New Mexico, USA. *Earth Sci. Rev.*, **79**, 141–162.

Mammerickx, J. & Klitgord, K.D. (1982) Northern East Pacific Rise: Evolution from 25 m.y. B.P. to the present. *J. Geophys. Res.*, **87**, 6751–6759.

Mancktelow, N.S. & Pavlis, T.L. (1994) Fold-fault relationships in low-angle detachment systems. *Tectonics*, **13**, 668–685.

Martín-Barajas, A., Stock, J.M., Layer, P., Hausback, B., Renne, P. & López-Martínez, M. (1995) Arc-rift transition volcanism in the Puertecitos volcanic province, northeastern Baja California, Mexico. *Geol. Soc. Am. Bull.*, **107**, 407–424.

Matchan, E. & Phillips, D. (2011) New $^{40}Ar/^{39}Ar$ ages for selected young (< 1 Ma) basalt flows of the Newer Volcanic Province, southeastern Australia. *Quat. Geochronol.*, **6**, 356–368.

Michaud, F., Royer, J.Y., Bourgois, J., Dyment, J., Calmus, T., Bandy, W., Sosson, M., Mortera-Gutiérrez, C., Sichler, B., Rebolledo-Viera, M. & Pontoise, B. (2006) Oceanic-ridge subduction vs. slab break off: Plate tectonic evolution along the Baja California Sur continental margin since 15Ma. *Geology*, **34**, 13–16.

Nagy, E.A., Grove, M. & Stock, J.M. (1999) Age and stratigraphic relationships of pre- and syn-rift volcanic deposits in the northern Puertecitos volcanic province, Baja California, Mexico. *J. Volcanol. Geoth. Res.*, **93**, 1–30.

Oskin, M. (2002) *Part I. Tectonic Evolution of the Northern Gulf of California, Mexico, Deduced from Conjugate Rifted margins of the Upper Delfin Basin; Part II. Active Folding and Seismic Hazard in Central Los Angeles, California*. PhD Thesis, California Institute of Technology, Pasadena.

Oskin, M. & Stock, J.M. (2003a) Pacific-North America plate motion and opening of the Upper Delfín basin, northern Gulf of California, Mexico. *Geol. Soc. Am. Bull.*, **115**, 1173–1190.

Oskin, M. & Stock, J.M. (2003b) Cenozoic volcanism and tectonics of the continental margins of the upper Delfín Basin, northeastern Baja California and western Sonora. In: *Tectonic Evolution of Northwestern México and the Southwestern USA. Geol. Soc. Am. Spec. Pup.* (Ed. by Johnson S.E., Paterson S.R., Fletcher J.M., Girty G.H., Kimbrough D.L. & Martín-Barajas A.) **374**, 421–438.

Osmundsen, P.T. & Andersen, T.B. (2001) The middle Devonian basins of western Norway: Sedimentary response to large-scale transtensional tectonics? *Tectonophysics*, **332**, 51–68.

Phillips, G., Wilson, C.J.L., Phillips, D. & Szczepanski, S.K. (2007) Thermochronological ($^{40}Ar/^{39}Ar$) evidence of Early Palaeozoic basin inversion within the southern Prince Charles Mountains, East Antarctica: Implications for East Gondwana. *Journal of the Geological Society*, **164**, 771–784.

Plattner, C., Malservisi, R., Dixon, T.H., LaFemina, P., Sella, G.F., Fletcher, J. & Suarez-Vidal, F. (2007) New constraints on relative motion between the Pacific Plate and Baja California microplate (Mexico) from GPS measurements. *Geophys. J. Int.*, **170**, 1373–1380.

Renne, P.R., Swisher, C.C., Deino, A.L., Karner, D.B., Owens, T.L. & DePaolo, D.J. (1998) Intercalibration of standards, absolute ages and uncertainties in $^{40}Ar/^{39}Ar$ dating. *Chem. Geol.*, **145**, 117–152.

Renne, P.R., Deino, A.L., Hames, W.E., Heizler, M.T., Hemming, S.R., Hodges, K.V., Koppers, A.A.P., Mark, D.F., Morgan, L.E., Phillips, D., Singer, B.S., Turrin, B.D., Villa, I.M., Villeneuve, M. & Wijbrans, J.R. (2009) Data reporting norms for $^{40}Ar/^{39}Ar$ geochronology. *Quat. Geochronol.*, **4**, 346–352.

Rothstein, D.A. & Manning, C.E. (2003) Geothermal gradients in continental magmatic arcs; constraints from the eastern Peninsular Ranges Batholith, Baja California, Mexico. In: *Tectonic Evolution of Northwestern México and the Southwestern USA. Geol. Soc. Am. Spec. Pap.* (Ed. by S.E. Johnson, S.R. Paterson, J.M. Fletcher, G.H. Girty, D.L. Kimbrough & A. Martín-Barajas), **374**, 337.

Sawlan, M.G. (1991) Magmatic evolution of the Gulf of California rift. *Am. Assoc. Pet. Geol. Mem.*, **47**, 301–369.

Schlische, R.W. (1993) Anatomy and evolution of the Triassic-Jurassic continental rift system, eastern North America. *Tectonics*, **12**, 1026–1042.

Schlische, R.W. (1995) Geometry and origin of fault-related folds in extensional settings. *Am. Assoc. Pet. Geol. Bull.*, **79**, 1661–1678.

Seiler, C. (2009) *Structural and Thermal Evolution of the Gulf Extensional Province in Baja California, Mexico: Implications for Neogene Rifting and Opening of the Gulf of California*. PhD Thesis, The University of Melbourne, Melbourne.

Seiler, C., Fletcher, J.M., Quigley, M.C., Gleadow, A.J.W. & Kohn, B.P. (2010) Neogene structural evolution of the Sierra San Felipe, Baja California: Evidence for proto-gulf transtension in the Gulf Extensional Province? *Tectonophysics*, **488**, 87–109.

Seiler, C., Fletcher, J.M., Kohn, B.P., Gleadow, A.J.W. & Raza, A. (2011) Low-temperature thermochronology of northern Baja California, Mexico: Decoupled slip-exhumation gradients and delayed onset of oblique rifting across the Gulf of California. *Tectonics*, **30**, TC3004.

Sözbilir, H., Sari, B., Uzel, B., Sümer, Ö. & Akkiraz, S. (2011) Tectonic Implications of Transtensional Supradetachment Basin Development in an Extension-Parallel Transfer Zone: The Kocaçay Basin, Western Anatolia. Turkey. *Basin Res.*, **23**, 423–448.

Spencer, J.E. (1985) Miocene low-angle normal faulting and dike emplacement, Homer Mountain and surrounding areas, southeastern California and southernmost Nevada. *Geol. Soc. Am. Bull.*, **96**, 1140–1155.

Steiger, R.H. & Jaeger, E. (1977) Subcommission on geochronology: Convention on the use of decay constants in geo- and cosmochronology. *Earth Planet. Sci. Lett.*, **36**, 359–362.

Stock, J.M. (1989) Sequence and geochronology of Miocene rocks adjacent to the Main Gulf escarpment: Southern Valle Chico, Baja California Norte, Mexico. *Geofísica Internacional*, **28**, 851–896.

Stock, J.M. (2000) Relation of the Puertecitos volcanic province, Baja California, Mexico, to development of the plate boundary in the Gulf of California. In: *Cenozoic Tectonics and Volcanism of Mexico. Geol. Soc. Am. Spec. Pap.* (Ed. by H. Delgado-Granados, G. Aguirre-Díaz & J.M. Stock) **334**, 143–156.

Stock, J.M. & Hodges, K.V. (1989) Pre-Pliocene extension around the Gulf of California and the transfer of Baja California to the Pacific plate. *Tectonics*, **8**, 99–115.

Stock, J.M. & Hodges, K.V. (1990) Miocene to Recent structural development of an extensional accommodation zone, northeastern Baja California, Mexico. *J. Struct. Geol.*, **12**, 315–328.

Stock, J.M., Lewis, C.J. & Nagy, E.A. (1999) The Tuff of San Felipe: An extensive middle Miocene pyroclastic flow deposit in Baja California, Mexico. *J. Volcanol. Geoth. Res.*, **93**, 53–74.

Topping, D.J. (1993) Paleogeographic reconstruction of the Death Valley extended region: Evidence from Miocene large rock-avalanche deposits in the Amargosa Chaos Basin, California. *Geol. Soc. Am. Bull.*, **105**, 1190–1213.

Umhoefer, P.J., Schwennicke, T., Del Margo, M.T., Ruiz-Geraldo, G., Ingle, J.C. & McIntosh, W. (2007) Transtensional fault-termination basins: An important basin type illustrated by the Pliocene San Jose Island basin and related basins in the southern Gulf of California, Mexico. *Basin Res.*, **19**, 297–322.

Yarnold, J.C. & Lombard, J.P. (1989) Litho-kinematic facies model for large landslide deposits in arid settings. *Am. Assoc. Pet. Geol. Bull.*, **73**, 554–555.

Yin, A. & Dunn, J.F. (1992) Structural and stratigraphic development of the Whipple-Chemehuevi detachment fault system, southeastern California: Implications for the geometrical evolution of domal and basinal low-angle normal faults. *Geol. Soc. Am. Bull.*, **104**, 659–674.

Manuscript received 29 February 2012; In revised form 10 September 2012; Manuscript accepted 14 September 2012.